## PRION DISEASE

# Structure-based drug design identifies polythiophenes as antiprion compounds

Uli S. Herrmann,[1] Anne K. Schütz,[2]* Hamid Shirani,[3]* Danzhi Huang,[4] Dino Saban,[1]† Mario Nuvolone,[1] Bei Li,[1] Boris Ballmer,[1] Andreas K. O. Åslund,[3]‡ Jeffrey J. Mason,[3] Elisabeth Rushing,[1] Herbert Budka,[1] Sofie Nyström,[3] Per Hammarström,[3] Anja Böckmann,[5] Amedeo Caflisch,[4] Beat H. Meier,[2] K. Peter R. Nilsson,[3] Simone Hornemann,[1]§ Adriano Aguzzi[1]§

Prions cause transmissible spongiform encephalopathies for which no treatment exists. Prions consist of PrP$^{Sc}$, a misfolded and aggregated form of the cellular prion protein (PrP$^C$). We explore the antiprion properties of luminescent conjugated polythiophenes (LCPs) that bind and stabilize ordered protein aggregates. By administering a library of structurally diverse LCPs to the brains of prion-infected mice via osmotic minipumps, we found that antiprion activity required a minimum of five thiophene rings bearing regularly spaced carboxyl side groups. Solid-state nuclear magnetic resonance analyses and molecular dynamics simulations revealed that anionic side chains interacted with complementary, regularly spaced cationic amyloid residues of model prions. These findings allowed us to extract structural rules governing the interaction between LCPs and protein aggregates, which we then used to design a new set of LCPs with optimized binding. The new set of LCPs showed robust prophylactic and therapeutic potency in prion-infected mice, with the lead compound extending survival by >80% and showing activity against both mouse and hamster prions as well as efficacy upon intraperitoneal administration into mice. These results demonstrate the feasibility of targeted chemical design of compounds that may be useful for treating diseases of aberrant protein aggregation such as prion disease.

## INTRODUCTION

Prions, infectious agents that cause transmissible spongiform encephalopathies, consist of PrP$^{Sc}$, a misfolded and aggregated form of the cellular prion protein (PrP$^C$) (1). The search for antiprion drugs has focused on compounds that reduce expression of PrP$^C$, interfere with the transition process of PrP$^C$ into PrP$^{Sc}$, dissociate PrP$^{Sc}$, or target the toxic cascades triggered by prion infection (2–4). Among the latter, compounds inhibiting the unfolded protein response (UPR) pathway or 3-phosphoinositide–dependent kinase-1 (PDK1) activity showed encouraging therapeutic activity (5, 6). However, because these compounds act on downstream effectors of neurodegeneration and display significant target-related toxicity, they are unlikely to be curative and may need to be combined with inhibitors of prion replication.

Antibodies to PrP$^C$ can prevent prion neuroinvasion (7), yet are less effective in therapeutic settings (8) and may cause acute toxicity (9, 10). Furthermore, most drug-like compounds showing prionostatic activity in vitro have failed in vivo because of poor bioavailability, toxicity, short metabolic half-life, or because their activity was limited to a narrow range of prion strains (11). "Compound B," IND24, and anle138b prolonged the life of mice infected with Rocky Mountain Laboratory (RML) prions by ~2-fold (12–15), but none have yet been shown ef-

fective against any human prion strain. Pentosan polysulfate (PPS) (16), thought to interfere with the conversion of PrP$^C$ to PrP$^{Sc}$, prolongs the survival of prion-infected mice in a strain-independent manner, but intraventricular administration of PPS to prion-affected patients was unsuccessful (17). Quinacrine raised high hopes because it clears PrP$^{Sc}$ from prion-infected cultured cells (18), yet was ineffective in human prion diseases (17, 19) and may foster drug resistance of prions (20), perhaps by promoting conformational changes (21). Doxycycline was once considered promising, yet a clinical trial found it to be ineffective (22). Hence, there is an alarming dearth of clinically effective antiprion compounds.

When evaluating amyloid-interacting compounds as potential therapeutic agents, one should consider that the frangibility (that is, the propensity to break up into fragments) of protein aggregates and oligomers may be deleterious rather than beneficial. Because the minimal infectious unit (the "propagon") (23) is thought to comprise a single aggregate of PrP, breaking down fibrils into a larger number of smaller units may actually accelerate the disease. Theoretical considerations and experimental data suggest that the frangibility of amyloid fibers is a crucial determinant of their infectiousness (24).

Luminescent conjugated polythiophenes (LCPs) are polymeric thiophene-based fluorescent molecules that preferentially bind to protein aggregates with repetitive cross-β sheet structures, including those formed by PrP$^{Sc}$, and can be used to stain many different amyloids in tissues (25–30). LCPs detect PrP$^{Sc}$ aggregates with greater sensitivity and specificity than Congo red, and their characteristic emission spectra can be exploited to differentiate distinct prion strains (29) and non-prion amyloids (28). Hence, LCP fluorescence spectra inform about the specific supramolecular conformation of many different protein aggregates. Monodisperse versions of LCPs with defined numbers of thiophene rings were found to discriminate protein aggregates better than heterodisperse mixtures (30–32). Crucially, LCP treatment of prion-infected

[1]Institute of Neuropathology, University Hospital of Zürich, University of Zürich, 8091 Zürich, Switzerland. [2]Physical Chemistry, Eidgenössische Technische Hochschule (ETH) Zürich, 8093 Zürich, Switzerland. [3]Department of Physics, Chemistry and Biology (IFM), Linköping University, 58183 Linköping, Sweden. [4]Department of Biochemistry, University of Zürich, 8057 Zürich, Switzerland. [5]Institut de Biologie et Chimie des Protéines, UMR 5086 CNRS/Université de Lyon 1, 69367 Lyon, France.
*These authors contributed equally to this work.
†Present address: Department of Neurosurgery, University Hospital Essen, 45147 Essen, Germany.
‡Present address: The Norwegian University of Science and Technology, 7491 Trondheim, Norway.
§Corresponding author. E-mail: adriano.aguzzi@usz.ch (A.A.); simone.hornemann@usz.ch (S.H.)

brain homogenates from mice and of cultured organotypic cerebellar slices reduced prion infectivity. This prionostatic effect seemed to rely on hyperstabilization, rather than dissociation, of PrP aggregates (33). A similar mechanism of hyperstabilization was hypothesized for the antiprion effect of thienyl pyrimidine derivatives (34).

Here, we tested the prophylactic and therapeutic value of LCPs in a mouse model of prion disease. We studied a chemically diverse library of LCPs and identified compounds that prolonged survival in prion-infected mice. We then used the results to derive structural features necessary for antiprion activity. Solid-state nuclear magnetic resonance (NMR) experiments and explicit solvent molecular dynamics simulations with model amyloids suggested that binding relied on the electrostatic interaction with several pivots per LCP. This allowed us to predict the efficacy of newly designed LCPs in in vivo experiments and to rationally design new LCPs with enhanced prophylactic activity and strain-independent therapeutic potency. Because LCPs are active against many amyloids, this strategy can be extended to proteinopathies beyond prion diseases.

## RESULTS

### Intraventricular infusion of four distinct LCPs in prion-infected mice

We first investigated the prophylactic efficacy of an "LCP mix" combining four LCPs (the heterodisperse compound LIN1001, as well as the chemically defined compounds LIN5001, LIN5002, and LIN7002) (Fig. 1A) in prion-infected wild-type CD1 mice and in PrP$^C$-overexpressing tga20 mice (35). To attain adequate local doses and circumvent brain penetrance issues, we administered compounds at a concentration of 4 mg/ml (ca. 5 mM) by continuous intraventricular infusion using osmotic minipumps, corresponding to 3.3 mg/kg per week. We implanted the pumps and started the infusions 1 week before intracerebral infection with RML6 (RML strain mouse-adapted scrapie prions, passage 6) prions [36 pg of total brain homogenate in 30 μl, corresponding to $3 \times 10^3$ median lethal dose (LD$_{50}$) units]. Depleted pumps were replaced with fresh ones at 35 days post-inoculation (dpi).

LCP mix–treated prion-infected wild-type CD1 mice (Fig. 1B) and tga20 mice (Fig. 1C) showed prolonged survival (+12%, $P = 0.0025$ and +25%, $P = 0.0004$, respectively; log-rank Mantel-Cox test) over vehicle-treated (PBS) prion-infected controls (table S1). None of the LCP mix–treated mice exhibited signs of acute toxicity. The diagnosis of prion disease was confirmed histologically and biochemically in all terminally diseased mice. Comparable levels of proteinase K–resistant PrP (PrP$^{Sc}$) were identified by Western blot analysis in the brains of vehicle- and LCP-treated mice (fig. S1, A and B). However, LCP-treated brains exhibited enhanced levels of PrP aggregates resistant to boiling in SDS (fig. S1, A and B), similar to prion-infected LCP-treated organotypic slice cultures (33). Quantification of PrP aggregates by the misfolded protein assay (33, 36–39) showed reduced levels in brains of LCP-treated wild-type CD1 mice (Fig. 1D) and tga20 mice (Fig. 1E and table S1), reflecting the efficiency of the LCP mixture in delaying disease progression.

### Intraventricular infusion of individual LCPs in prion-infected mice

To evaluate the antiprion activity of the individual LCPs, we administered LCP mix and each single LCP (LIN1001, LIN5001, LIN5002,

and LIN7002; 3.3 mg/kg per week each) to tga20 mice (Fig. 1F). Treatment was started prophylactically 7 days before intracerebral injection of RML6 prions (3.6 μg of brain homogenate in 30 μl, corresponding to $3 \times 10^5$ LD$_{50}$ units). Mice treated with LCP mix showed prolonged survival (+20.5%, $P = 0.0007$), indicating that this treatment was efficient even after inoculation of a 100-fold higher prion load. LIN5001 (+36.4%, $P = 0.031$) and LIN7002 (+16.7%, $P = 0.007$) showed the highest efficacy in prolonging survival, whereas LIN5002 had no effect. LIN5001 and LIN7002 differ from LIN5002 by the presence of biterminal anionic groups, suggesting that these moieties are essential to their antiprion properties. LIN1001 was not only ineffective but also caused acute toxicity including convulsions and sudden death.

LCP treatment did not affect brain PrP$^{Sc}$ levels, except for LIN7002, which caused a modest PrP$^{Sc}$ reduction. Conversely, all LCPs, regardless of their antiprion potency, induced SDS-stable PrP$^{Sc}$ aggregates (including prominent dimers and trimers), suggestive of aggregate hyperstabilization (fig. S1C). As in the previous experiment, the misfolded protein assay revealed decreased numbers of PrP aggregates in LCP-treated mice (Fig. 1G). Total PrP was unaffected by treatment with therapeutically effective and ineffective LCPs (fig. S1D).

### LIN5001 treatment in the presymptomatic and clinical stage of prion disease in mice

Having identified LIN5001 as the most effective compound of this series, we asked whether the survival of prion-infected mice could also be increased by administering LIN5001 in a therapeutic regimen, that is, when administered after prion infection rather than prophylactically. When started at 20 dpi, LIN5001 treatment prolonged the survival time after infection (incubation time) by +20.5% ($P = 0.0036$) compared to vehicle-treated (median, 66 days) or non-operated animals (median, 65 days; Fig. 1H). Even when treatment was first started at 50 dpi (Fig. 1I), that is, in the presence of advanced disease with clinically overt neurological signs (tail rigidity and hindlimb paresis), there was a trend toward increased survival compared to vehicle-treated and non-operated prion-infected mice (+7.3%, $P = 0.12$ and +13.1%, $P = 0.014$, respectively). Western blots confirmed the presence of proteinase K–resistant PrP$^{Sc}$ in the brains of all prion-infected mice (fig. S1, E and F) and of SDS-stable PrP$^{Sc}$ oligomers even when using an increased proteinase K concentration (fig. S1G). The readings of the misfolded protein assay, which are a quantitative measure of protein aggregates, were decreased in the brains of LIN5001-treated mice (Fig. 1J).

### Defining the structure-activity relationship of LCPs

Next, we explored the chemical space of LCPs by designing a library of new compounds with a conjugated backbone but differing in their terminal groups or in the backbone length, as well as selenophenes with constrained backbone flexibility (Fig. 2A). These new LCPs were tested in a prophylactic regimen (Fig. 2B). Replacement of the terminal carboxyl groups by aldehyde residues (LIN5032) abolished all antiprion efficacy (median, 63 days; $P = 0.66$), and ketone group substitution (LIN5029) greatly reduced it (median, 68.5 days; +6%, $P = 0.015$; Fig. 2B). Elongation of the LCP backbone with two thiophene rings (LIN7001) resulted in similar efficacy (median, 82 days; +27%, $P = 0.04$) as LIN5001 (median, 78 days; +20.9%, $P = 0.0002$). Because replacement of sulfur with selenium enhances the axial rigidity of LCPs (40, 41), we replaced the central or the two terminal thiophenes of LIN5001 and LIN5002 with selenophenes (LIN5050 and LIN5051, respectively). Similar to its ineffective thiophene counterpart,

**Fig. 1. Treatment with thiophene-based compounds extends the survival time of prion-infected mice.** (**A**) Molecular structures of the compounds contained in the "LCP mix." All LCPs were polyanionic. LIN1001 consists of heterodisperse polymers ($n$ = 11 to 20), whereas LIN5002, LIN5001, and LIN7002 are monodisperse; the first digit indicates the number of thiophene groups. Da, dalton; MW, molecular weight. (**B** and **C**) Survival curves of RML6-infected CD1 mice (B; $n$ = 8) and tga20 mice (C; $n$ = 7) prophylactically treated with LCP mix (4 mg kg$^{-1}$) or vehicle [phosphate-buffered saline (PBS); $n$ = 4 in each series]. LCP mix–treated wild-type (B) and tga20 mice (C) showed a +12 and +25% life extension, respectively ($P$ = 0.0025 and $P$ = 0.0004, respectively; log-rank Mantel-Cox test was used for survival analyses; details in table S1). (**D** and **E**) The misfolded protein assay showed reduced PrP aggregates in brains of LCP mix–treated prion-infected wild-type CD1 mice (left) (D) and tga20 mice (right) (E). Negative control, brain homogenate of non-infected mice (NBH). Data are means ± SEM of relative light units (RLU) mg$^{-1}$ of total protein.\*$P$ < 0.05; \*\*$P$ < 0.01; \*\*\*$P$ < 0.001; Student's $t$ test. (**F**) Survival of RML6-infected tga20 mice treated prophylactically with LCP mix or individual LCPs (4 mg kg$^{-1}$). LCP mix, LIN7001, and LIN5001 (but not LIN5002 or LIN1001) extended survival compared to vehicle controls. Each group included six mice. (**G**) Brain PrP aggregates in RML6-infected mice, measured by the misfolded protein assay, were reduced by efficacious LCPs and, to a lesser extent, by the ineffective compound LIN5002. For all multiple comparisons of misfolded protein assay data, one-way analysis of variance (ANOVA) with Dunnett's posttest was used.



(**H**) Significantly prolonged survival of RML6-infected tga20 mice treated with LIN5001 starting in the presymptomatic phase at 20 dpi (+21%; $n$ = 9) compared to vehicle-treated and non-operated mice ($n$ = 7 and $n$ = 10, respectively). (**I**) Same as (H) with LIN5001 treatment started in the symptomatic phase (50 dpi) showing a trend (+7.3%; $n$ = 8) toward extended survival (vehicle-treated mice, $n$ = 8). (**J**) Misfolded protein assay showing reduced PrP aggregates in brains of prion-infected mice treated with LIN5001 starting at 20 dpi, compared to vehicle-treated (\*$P$ < 0.05) and untreated (\*\*$P$ < 0.01) mice. One-way ANOVA with Dunnett's posttest was used for statistical analysis.
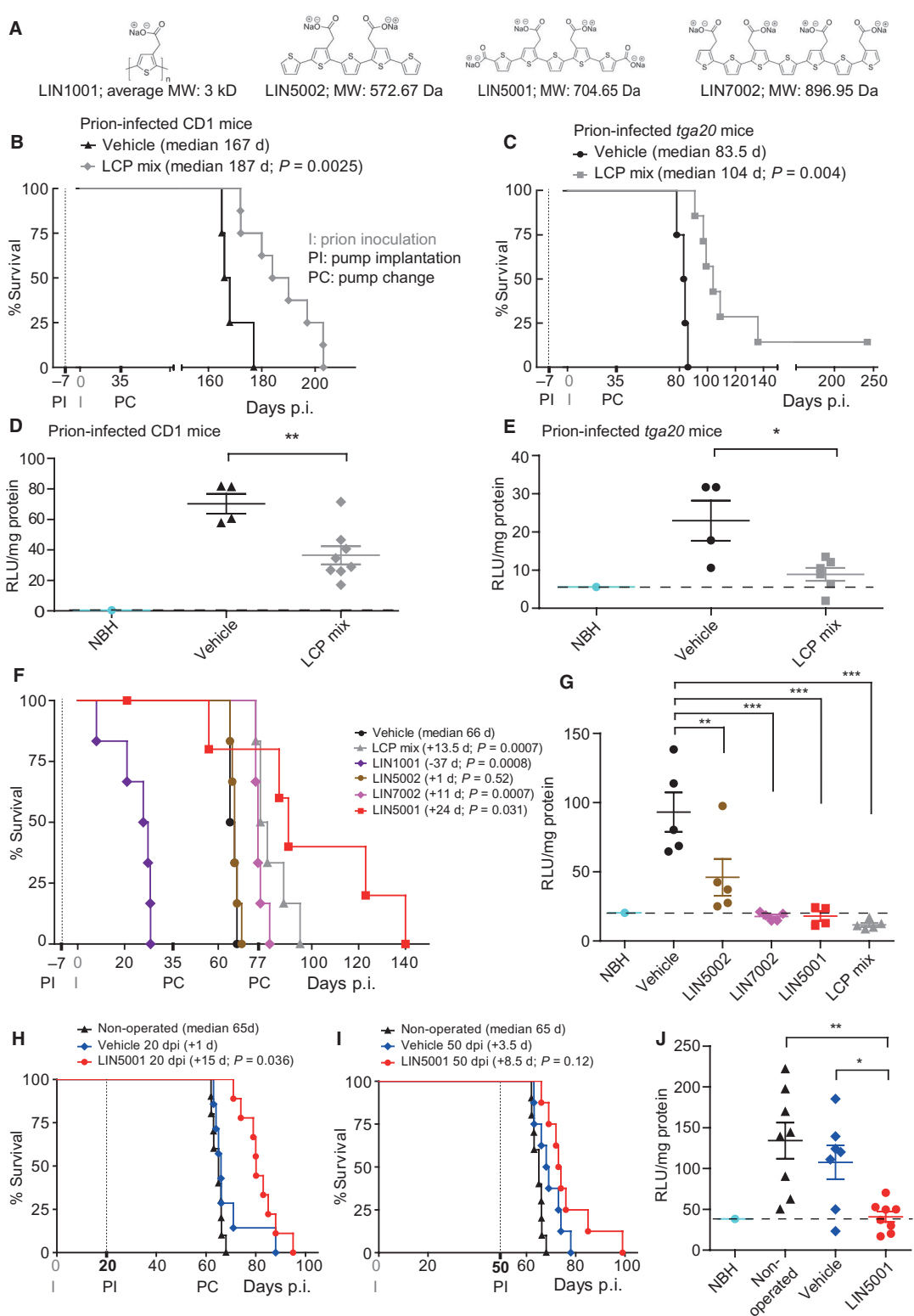
**Fig. 2. Potency of rationally designed LCPs.** (**A**) Structures of rationally designed LCPs. (**B**) LIN5001 (+20.9%; *n* = 7), LIN7001 (+27.1%; *n* = 7), and LIN5050 (+57.3%; *n* = 11) significantly increased survival of RML6-infected *tg*a20 mice compared to vehicle-treated mice (*n* = 6), whereas LIN5029 (*n* = 6) had only a marginal (+6.2%) effect. LIN5032 (*n* = 7), LIN5002 (*n* = 7), and LIN5051 (*n* = 7) had no effect on survival. Three mice treated with LIN5050 died prematurely for undetermined reasons. Log-rank Mantel-Cox test was used for survival analyses. (**C**) Western blot analyses of brain homogenates from prion-infected (RML+) and non-infected (RML−) *tg*a20 mice treated with LCPs as indicated. PK+, predigested with proteinase K; PK−, not digested with proteinase K. (**D**) Same as (C), but without proteinase K digestion. Antibody POM1 was used for PrP detection in all Western blots presented in this study. Loading control, β-actin. (**E**) PrP aggregates in the brain homogenates of LIN7001-treated RML6-infected mice were significantly reduced, whereas the other LCPs showed a trend toward reduction of PrP aggregates as measured by the misfolded protein assay. One-way ANOVA with Dunnett's posttest was used for statistical analysis. (**F**) Western blot analyses for PrP of differentially fractionated brain homogenates from non-infected (NBH) and prion-infected mice treated with vehicle, LIN5002, or LIN5001 (density gradient ultracentrifugation, OptiPrep 10 to 40%). The samples of the vehicle- and LIN5002-treated animals elicited most of the signal in the lower (1–5) and higher fractions (11–14). Prion-infected mice treated with LIN5001 showed reduced signals in fractions 11 to 14. (**G**) Quantification of ultracentrifugation studies using three biological replicates per condition (mean ± SEM). (**H**) HADDOCK model of LIN5001 docked to HET-s(218–289)$^{E265K}$ based on NMR-derived distance restraints (table S2). The two key residues for binding, K$^{229}$ and K$^{265}$, are marked in two different shades of blue. Four of 10 lysine residues are occupied by carboxylic acid side-chain groups of LIN5001. Two visualizations from different angles, illustrating the details of the interaction between LCP and amyloid, are shown.
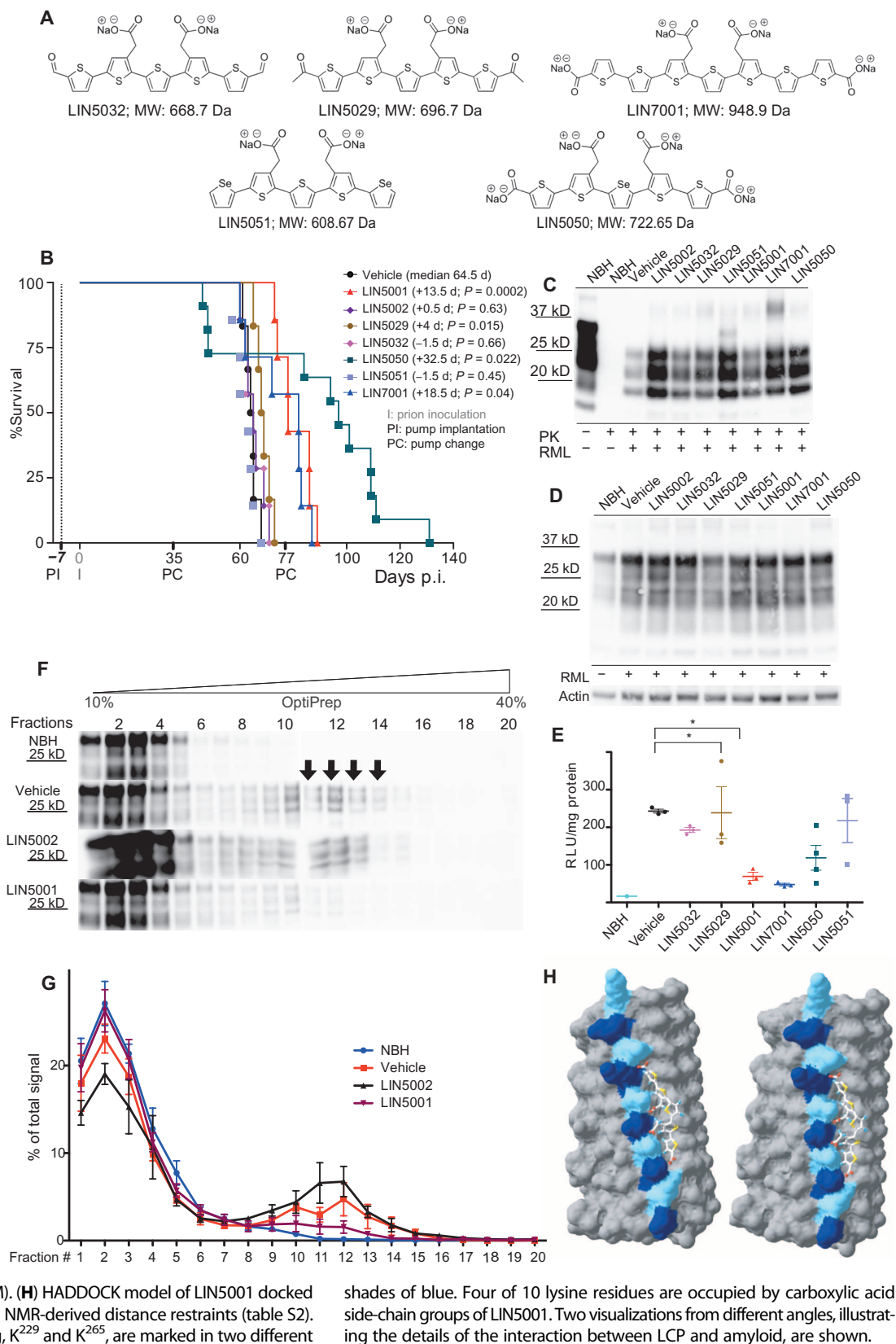
LIN5002, the selenophene LIN5051 had no antiprion effect (median, 63 days; $P = 0.45$; Fig. 2B). Conversely, LIN5050, the thioselenophene variant of LIN5001, delayed the disease (median, 97 days; +50.3%, $P = 0.021$; Fig. 2B), although three mice died prematurely for undetermined reasons. These results confirmed that the terminal carboxyl groups are important for in vivo therapeutic potency of both thiophenes and thioselenophenes.

PrP$^{Sc}$ and total PrP were present at similar levels in brains of terminally sick vehicle- and LCP-treated mice, and most LCPs induced SDS-stable oligomers (Fig. 2, C and D, and fig. S1, H and I). However, LIN5001-treated brains showed slightly decreased PrP deposition and gliosis (fig. S2), and revealed reduced readings in the misfolded protein assay, roughly reflecting the therapeutic efficacy of the respective LCPs (Fig. 2E).

To gain insight into the relationship between treatment and PrP aggregation states, we performed density gradient ultracentrifugation experiments using rate-zonal separation, which differentiates particles according to their size and shape (42, 43). Brain homogenates of non-infected mice and of RML-infected mice treated with either vehicle, LIN5001, or the ineffective compound LIN5002 were fractionated over a 10 to 40% OptiPrep density gradient, and fractions were analyzed by Western blotting for total PrP. In RML-infected mice treated with vehicle or LIN5002, most PrP was detected in the lowest and higher fractions (fractions 1 to 5 and 11 to 14; Fig. 2, F and G). Conversely, PrP from prion-infected mice treated with LIN5001 migrated almost exclusively with fractions 1 to 5. Quantification of three biological replicates (Fig. 2F and fig. S3) for each group (three independent ultracentrifugation runs using 10 to 40% OptiPrep density gradients) revealed a strong reduction in high–molecular weight species (thought to represent oligomeric PrP aggregates) in brain homogenates of LIN5001-treated mice (Fig. 2G).

We then performed another fractionation experiment using a 5 to 20% OptiPrep density gradient (fig. S4). Again, most PrP in RML-infected mice treated with vehicle or LIN5002 was detected in fractions 1 to 8 and 19 to 20, whereas samples from prion-infected mice treated with LIN5001 showed again a strong reduction in higher–molecular weight species. These results strongly support our hypothesis that LIN5001 intervenes at early stages of the aggregation process by stabilizing small PrP$^{Sc}$ aggregates, possibly preventing their disassembly and inhibiting secondary nucleation.

## LCP binding at atomic resolution
Because the precise structure of PrP$^{Sc}$ is unknown, we based our structure-activity relationship (SAR) studies on the assumption of an in-register β sheet conformation, for which most experimental evidence exists (44–46). We opted to approximate the latter with the prion-forming domain of the fungal HET-s prion, the only self-propagating amyloid whose atomic structure has been solved. Although the amino acid sequence of PrP and HET-s diverge, we reasoned that the empirical congruence of therapeutic efficacy with the SAR predictions might vindicate the validity of our choice.

We therefore investigated the binding of LIN5001 to HET-s aggregates by solid-state NMR spectroscopy. HET-s(218–289) oligomers behave as prions, have a fully assigned NMR spectrum, and represent one of the structurally best-defined amyloids; HET-s(218–289) forms a β solenoid with two turns per molecule (47). Like PrP$^{Sc}$ fibrils, HET-s(218–289) prions are intensely stained by Congo red; Congo red binding relies on the electrostatic interaction between the negatively charged sulfonate groups of Congo red and the positively charged lysine residues on every fourth β strand on the HET-s(218–289) amyloid as well as the presence of a pronounced groove on the amyloid surface at the site of an arc between two β sheets (48). To mimic a parallel in-register β sheet representative for an amyloid with a single molecule per turn, we produced the E265K mutation of HET-s(218–289) that features a lysine ladder with a 4.8-Å spacing between lysines, including the ones involved in binding to Congo red (48).

The two-dimensional (2D) NMR spectra [proton-driven spin diffusion (PDSD)] of wild-type HET-s(218–289) and of HET-s(218–289)$^{E265K}$ (fig. S5A, black and blue) were superimposable except at the site of the mutation, indicating that they share an identical fold. We measured chemical shift perturbations (CSPs) and direct polarization transfer (PT) from LIN5001 to the residues of wild-type HET-s(218–289) and of HET-s(218–289)$^{E265K}$. Neither CSP nor PT was detected in the wild-type spectrum (fig. S5B), whereas the addition of LIN5001 to the E265K mutant elicited strong CSP and PT peaks similar to those observed for Congo red (fig. S5, C and D), indicating a high-affinity binding site and characterizing it by 15 specific experimental restraints.

To identify the binding mode, the CSP and PT data were translated into distance restraints from which a model was generated using HADDOCK docking (49) (Fig. 2H and table S2). Binding of the four unequally spaced negatively charged carboxyl groups of LIN5001 to the positively charged lysines of the mutant was best modeled by a $K^{229}/K^{229}/K^{265}/K^{265}$ pattern involving three HET-s molecules with a total of six β strands and a binding mode similar to Congo red but with a 10 Å/5 Å/10 Å distance pattern between the partnering residues on the different β sheets. In wild-type HET-s, position 265 is occupied by a glutamate instead of a lysine residue, thus precluding a sterically favorable 10 Å/5 Å/10 Å interaction with the carboxyl groups of LIN5001. This explains why NMR failed to detect binding of LIN5001 to wild-type HET-s (50). These docking data suggest that the binding of LIN5001 exploits the steric complementarity between its negative charges spaced at 5 and 10 Å in a "regioregular" pattern and the positive charges on the amyloid surface. In the simplest case, these conditions exist on each β strand of in-register parallel β sheet aggregates with surface-exposed arginine (R) and lysine (K) side chains (48), and define the minimal structural features necessary for LCP binding to prions.

## Molecular dynamics simulations to predict the binding of the LCPs to fibrils
The above observations defined the minimal structural features necessary for LCP binding to prions. We therefore created a number of LCPs with negative charges regularly spaced at about 5 Å and used the umbrella sampling simulation protocol to calculate the free energy profile of their binding to a model amyloid. The simplest instance of an amyloid satisfying the requirement of repetitive positive charges along the fibril axis exists in fibrils composed of in-register parallel β sheet strands with surface-exposed arginine (R) and lysine (K) side chains. This is congruent with a plausible structural model of PrP$^{Sc}$ predicting an in-register β sheet core extending between residues ~166 and 220 (44) and rich in K and R residues.

We therefore devised a minimal LCP binding site consisting of eight tripeptides (S-A-K) arranged in a parallel in-register β sheet (Fig. 3A). The initial coordinates were derived from the HET-s(218–289) NMR structure [Protein Data Bank (PDB) code 2LBU], in which the docked Congo red lies in a groove perpendicular to the solenoid β sheet. The groove originates from parallel β strands of alternating S$^{227}$-A$^{228}$-K$^{229}$

**Fig. 3. Atomistic simulations to design new LCPs with enhanced antiprion properties in vivo.** (**A**) In-register parallel β sheet consisting of eight 3-residue peptides used to compute the free energy profile of binding. The unbinding pathway used for the umbrella sampling protocol was determined by pulling the center of the LCP in the direction shown by the arrow with a velocity of 5 nm/ns. (**B**) For each LCP, except for LIN5050 and LIN5051 (because of missing parameters in the CHARMM force field for selenium-containing molecules), the free energy profile of binding to the model peptide T-A-K was calculated using the umbrella sampling molecular dynamics protocol and the weighted histogram analysis method (*79*). Abscissa, distance of the LCP center of mass from the bound state; *W*, average reversible thermodynamic work done by the mean force along the distance. Free energy profiles were shifted vertically to overlap at the bound state, so that relative affinities could be inferred from the plateau corresponding to the unbound state (distance, >0.8 nm). (**C**) Structural stability of in-register parallel β sheets consisting of eight hexapeptides (ITIKQH) containing the TIK motif as binding groove, in the absence and presence of LCP LIN5001 (mean, 2.2; $P = 0.000022$) and LIN5044 (mean, 1.8; $P = 0.000000018$). Each bar reflects the number of strands, that is, hexapeptides, in the β sheet averaged over the final snapshots of 30 independent runs of 20 ns each. These results support the conjecture that LCPs hyperstabilize amyloid fibrils. (**D**) Molecular structures of LCPs selected from in silico predictions for in vivo testing. (**E**) Free energy profiles as a function of the distance from the bound state of selected LCPs into octameric T-A-K in-register parallel β sheets. (**F**) The strong binders LIN5044 (*n* = 6), LIN5045 (*n* = 6), and LIN7004 (*n* = 5) extended the survival of prion-infected mice compared to vehicle-treated controls (*n* = 7) by up to 87.5%, whereas treatment with the weaker binders LIN4027 (*n* = 7), LIN4003 (*n* = 7), and LIN5043 (*n* = 6) was ineffective. Log-rank Mantel-Cox test was used for survival analyses. (**G**) Western blot of brain samples from prion-infected and LCP-treated *tg*a20 mice. (**H**) Misfolded protein assay showing significant reduction of PrP aggregates in brains of LCP-treated prion-infected mice. One-way ANOVA with Dunnett's posttest was used for statistical analysis. ns, not significant. (**I**) Western blot of standard prion inoculum exposed to increasing concentrations of LIN5044 showing concentration-dependent stabilization of aggregates. Di-, mono-, and non-glycosylated PrP are indicated by black arrows and higher-order SDS-stable species by a gray arrow. (**J**) Western blot of rPrP fibrils incubated with LIN5044.
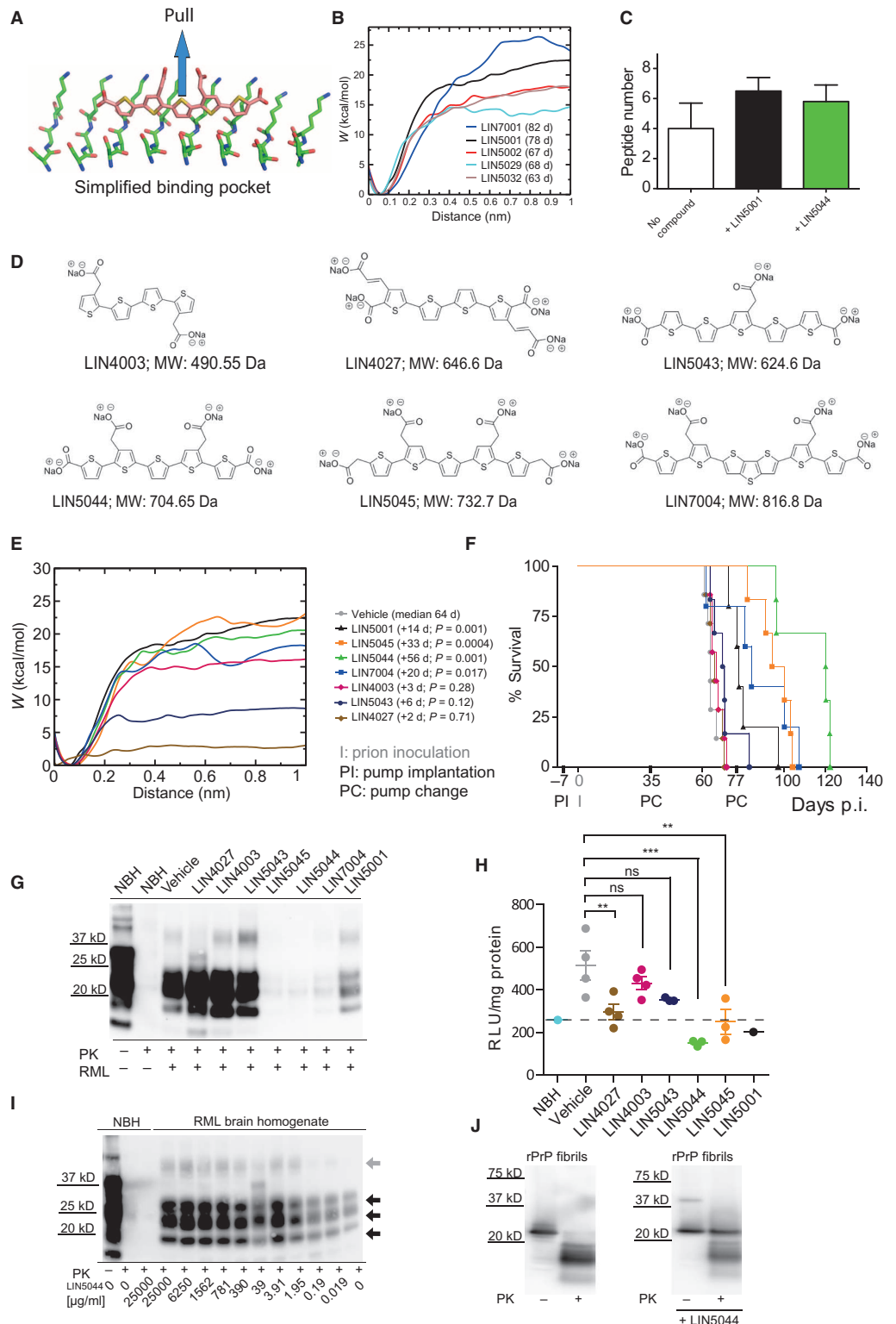
and $S^{263}$-$V^{264}$-$E^{265}$ segments. The backbones of the central residues (Ala$^{228}$ and Val$^{264}$) form the floor of the groove, whereas the side chains of residues S$^{227}$/S$^{263}$ and K$^{229}$/E$^{265}$ form the walls. To generate the initial parallel in-register β sheet arrangement of eight S-A-K peptides, residues V$^{264}$ and E$^{265}$ were changed to Ala and Lys, respectively, using visual molecular dynamics (51). S-A-K yielded a high binding affinity, supporting the validity of our calculations. On the basis of the PrP sequence between codons 178 to 212, seven further putative binding sites were selected and modeled by the octameric tripeptides (X-A-R/K): M-A-K, E-A-K, D-A-K, T-A-K, H-A-K, M-A-R, and V-A-R. The side chains of K and R provided positive charges, whereas A was chosen to model the groove of the fibril and X represents residues at the ±2 positions of K or R from the PrP sequence between codons 178 to 212. We then calculated the free energy profiles of LIN5001 binding to the various model fibrils (fig. S6A). The model consisting of octameric T-A-K yielded the most favorable binding free energy for LIN5001 and was used for all further calculations (movies S1 and S2). For octameric D-A-K, LIN5001 became unbound within 10 ns and was therefore not included in the graph.

The free energy profiles of binding of the LCP that had been tested in vivo (Fig. 3B) were consistent with the experimental data. Strikingly, the strongest binders (that is, LIN5001 and LIN7001) were also the most efficacious antiprion molecules. The in silico regio-specific interactions between the carboxylic groups of LIN5001 and the lysine side chains of the S/T-A-K groove were congruent with the interactions between the HET-s prion and the LIN5001 observed by NMR (Fig. 2H). In addition, multiple unrestrained molecular dynamics runs were carried out starting from a parallel in-register β sheet consisting of eight hexapeptides (I-T-I-K-Q-H, with the T-I-K motif forming a binding groove) in the "apo" form and bound to LIN5001 or LIN5044. These unbiased simulations revealed that LIN5001 and LIN5044 enhance the structural stability of the octameric I-T-I-K-Q-H β sheet (Fig. 3C).

The structural stability of in-register parallel β sheet oligomers consisting of eight copies of the 177–216 segment of the mouse prion protein was investigated by explicit solvent molecular dynamics in the absence and presence of LIN5001 (fig. S7A). The initial conformation was prepared using the PIRIBS-A model as previously reported (46). Three copies of LIN5001 were manually docked into the groove between residues T$^{183}$-I$^{184}$-K$^{185}$, T$^{192}$-T$^{193}$-K$^{194}$, and K$^{204}$-M$^{205}$-M$^{206}$ or R$^{208}$-V$^{209}$-V$^{210}$, respectively. Multiple independent simulations of 100 ns each were carried out for each system using different random assignments of the initial velocities. The CHARMM36 force field was used, and the temperature was kept constant at 310 or 360 K to enhance the sampling (fig. S7B). The distance between the C-α atoms of the neighboring residues (K$^{185}$, K$^{204}$, or R$^{208}$) was significantly shorter ($P < 0.01$) in the presence of LIN5001, providing support to the conjecture that LIN5001 stabilizes ordered in-register parallel β sheet oligomeric assemblies.

To investigate whether LCPs might also stabilize other amyloid structures, we carried out explicit solvent molecular dynamics simulations of eight copies of the Aβ$_{10-20}$ peptide segment (octameric Aβ$_{10-20}$) in the presence and absence of LIN7001. The hendecapeptide (11-mer) segment Aβ$_{10-20}$ includes the basic side chain of K$_{16}$ as well as the hydrophobic and amyloidogenic stretch L$_{17}$VFF$_{20}$. The starting conformation was the parallel in-register β sheet arrangement extracted from the solid-state NMR structure of the Osaka mutant of Aβ40 (PDB code 2MVX). The simulation protocol was identical to that for the molecular dynamics runs of the multimeric prion segments, and two independent 200-ns runs were performed for each of the apo structures and the structure with bound LIN7001. The structural stability of the octameric β sheet was higher in the presence of LIN7001, particularly at the N-terminal region, which showed significant fluctuations only in the apo simulations (fig. S8 and movies S3 and S4).

## Binding affinities of LCPs to in vitro–generated recombinant PrP fibrils

Next, we measured the dissociation constants ($K_d$) of LCPs bound to bona fide PrP fibrils and compared them to the free energy of in silico binding. $K_d$ values were determined by titrating LCPs against fibrils of recombinant mouse PrP (residues 23 to 231, rPrP, 5 μM). For each dilution step, fluorescence excitation spectra were recorded. Upon binding to the rPrP fibrils, LCPs underwent conformational changes that induced a shift of the excitation maximum (Exc$_{max}$), toward longer wavelengths, as well as increased fluorescence intensity (fig. S9A). The binding curves for distinct LCPs were generated by plotting the normalized ratio Exc$_{max}$(bound)/Exc$_{max}$(unbound) against the LCP concentration (fig. S9B). $K_d$ values were obtained by fitting the curves to a hyperbola function. LIN5044, among the strongest binders identified in silico, displayed the lowest $K_d$ and therefore the highest affinity (fig. S9A and table S3). The remaining LCPs showed intermediate $K_d$ values (table S3) with a ranking that was mostly congruent with in silico predicted binding energies.

## In vivo testing of in silico predicted LCPs

On the basis of the above results, 14 molecules (Fig. 3D and fig. S10) were selected for in silico testing from a library of 50 LCPs, and their free binding energy profiles were predicted using the octameric tripeptide model (Fig. 3E and fig. S6, C to E). These simulations led us to evaluate the in vivo antiprion activity of six compounds having four (LIN4027 and LIN4003), five (LIN5043, LIN5044, and LIN5045), and seven (LIN7004) thiophene rings. The free energy profiles of the LIN4027, LIN4003, and LIN5043 predicted a lower affinity than the ones for LIN5001 and LIN7001 (Fig. 3E), which may translate into poor in vivo efficacy. In contrast, the free energy profiles of the five-ring LIN5045 and LIN5044 as well as the seven-ring LIN7004 predicted high-affinity binding and potentially better in vivo efficacy.

Six LCPs (Fig. 3D) selected by their in silico properties were administered prophylactically to *tga20* mice infected with RML6 prions. As predicted by the molecular dynamics simulation, LIN4027, LIN4003, and LIN5043 did not prolong survival over vehicle-treated animals (median, 64 days; Fig. 3F). Instead, the strong binder LIN5044 was found to be the most efficient of the entire series. Survival was prolonged by 87.5% (median, 120 days; $P = 0.001$). LIN5045 and LIN7004, which were predicted to bind to fibrils efficiently, prolonged survival by 51.6% (median, 97 days; $P = 0.0004$) and by 31.25% (median, 84 days; $P = 0.017$), respectively. As a further control, LIN5001 was again effective in this series, prolonging survival time by 21.8% (median, 78 days; $P = 0.001$). Western blots of brain homogenates of LCP-treated RML6-infected animals displayed strongly reduced PrP$^{Sc}$ signals in mice treated with strong binders (LIN5045, LIN5044, and LIN7004; Fig. 3G and fig. S1, J and K), whereas total PrP levels were not affected (fig. S6F). Misfolded protein assay of brain homogenates evidenced a reduction in the signal that correlated with the antiprion efficiency of the respective LCPs, with LIN5044 decreasing the signal most effectively (Fig. 3H).

Preincubation of RML6-infected brain homogenates with increasing concentrations of LIN5044 and of rPrP fibrils with LIN5044 in vitro increased resistance of PrP to proteinase K (Fig. 3, I and J), in agreement with the notion that LCPs exert their antiprion effect by stabilizing PrP oligomers and with our in silico findings (Fig. 3C). As with PrP$^{Sc}$ and rPrP fibrils, incubation of HET-s(218–289)$^{E265K}$ fibrils with LIN5044 enhanced the levels of SDS-stable higher–molecular weight species (fig. S11). Histological analyses of the brains of mice treated with the most efficient compound LIN5044 revealed an overall reduction in spongiosis, PrP deposition, and astrogliosis at the terminal stage of the disease, suggesting attenuation of the neurodegenerative process (fig. S12).

## Therapeutic potency of LIN5044

To determine the upper limit of its therapeutic potential, lead compound LIN5044 was administered intraventricularly or intraperitoneally to prion-infected mice that had progressed to the symptomatic phase of the disease. The latter was determined by monitoring a cohort of noninfected and prion-infected tga20 mice for motor performance using rotarod assays. A significant decline in performance became evident at 48 dpi (fig. S13A). On the following day (49 dpi), prion-infected tga20 mice were randomly assigned to one of the following treatment arms: LIN5044 (intracerebrally), vehicle (intracerebrally), LIN5044 (intraperitoneally) (400 μg in 100 μl of PBS, three times weekly), or vehicle (intraperitoneally). LIN5044, administered intracerebrally or intraperitoneally, significantly prolonged survival (+21.8%, $P = 0.0018$ and +14.5%, $P = 0.044$, respectively; median survival of vehicle-treated mice, 66.5 days; Fig. 4, A and B). Brain immunoblots from mice treated with LIN5044 revealed the presence of SDS-stable oligomers and slightly reduced PrP$^{Sc}$ (Fig. 4, C and D), whereas PrP$^{C}$ was not reduced (fig. S13, B and C).

The effectiveness of antiprion compounds is often limited to specific prion strains; compound B inhibits the propagation of RML but not of 263K prions (13). We therefore asked whether LIN5044 would be beneficial to tg81 mice overexpressing Syrian hamster Prnp (52) infected with hamster-adapted 263K prions (53). Intraperitoneal administration of LIN5044 starting at 20 dpi (400 μg in 100 μl, three times weekly) delayed the progression to the end stage of the disease by +13.1% over vehicle-treated controls (median, 69 days; $P < 0.0003$; Fig. 4E). Western blots revealed reduced PrP$^{Sc}$ levels and SDS-stable oligomers (Fig. 4F). PrP levels were again not affected (fig. S13D). Hence, treatment with LIN5044 is efficient also in tg81 mice infected with 263K prions.

To explore the efficacy of lead compound LIN5044, we sacrificed a cohort of tga20 mice infected with 3.6-μg of RML6 brain homogenate in 30 μl intracerebrally, corresponding to $3 \times 10^5$ LD$_{50}$ units, that had received prophylactic LIN5044 or vehicle treatment. At 63 dpi, vehicle-treated mice were approaching the terminal stage of the disease (median survival at this dose of RML6 prion, 64 days). However, LIN5044-treated mice lacked overt clinical signs and showed no discernible or strongly reduced spongiosis and neuronal cell loss (Fig. 4G).

As a further model of prion propagation, we assessed the capacity of brain homogenates to seed the fibrillation of rPrP in vitro. Brain homogenates from RML6-infected, vehicle-treated mice (terminally sick and sacrificed at 63 dpi; fig. S14, A and B) induced rPrP fibril formation in all samples, whereas Prnp$^{-/-}$ brain homogenates did not seed. However, the seeding capacity of brain homogenates from LIN5044-treated mice sacrificed at 63 dpi was conspicuously depleted (11% conversion), whereas brain homogenates from terminally sick LIN5044-treated mice exhibited the same seeding potency as homogenates from terminally sick vehicle-treated mice (fig. S14, A and C). These results imply that LIN5044 delays prion replication in vivo and adds to the evidence that LIN5044 mitigates the disease by reducing the efficiency of prion self-perpetuation.

## DISCUSSION

Rational drug design requires detailed understanding of the interactions between compounds and their targets. Because the structure of PrP$^{Sc}$ is unknown, such understanding was approximated with a variety of structural and computational approaches. PrP$^{Sc}$ is hypothesized to form a β-helix fold (54), a spiral (55), or a parallel in-register β sheet (44, 46, 56), with the latter model being supported by most experimental evidence (45). The mutant fungal prion HET-s(218–289)$^{E265K}$ was selected as a plausible structural proxy, because it represents the only available high-resolution structure of a prion and its stacked lysine residues are arranged in a single-layer repeat amyloid as expected for PrP$^{Sc}$.

LCP binding to HET-s(218–289)$^{E265K}$ relies on electrostatic pivots created by positively charged lysines, arranged with a periodicity of 4.8 Å along the major axis of the amyloid fibrils, and similarly spaced negative charges on the LCPs. Although each individual interaction is weak, because of desolvation and entropic penalties, the repetitive nature of both stacked lysines within the β sheet and thiophene moieties results in cooperative, high-avidity binding.

We simulated in silico the binding of LCPs to a parallel in-register β sheet model and correlated their computed binding energies to their antiprion efficacy in vivo. Gratifyingly, the LCPs displaying the most favorable binding energies were the therapeutically most effective ones. Crucially, when the model was used to instruct the de novo design of additional LCPs, the estimated binding energies were predictive of antiprion activity in vivo. Therefore, molecular dynamics simulation of binding to fibrils allows for the design and optimization of antiprion compounds.

The above results allowed us to extract a set of rules that predicted the activity of LCPs. First, the backbone must contain at least five thiophene or selenophene moieties, because two LCPs consisting of only four thiophene moieties had no antiprion activity. A conjugated backbone consisting of ≥5 thiophene moieties is also required to detect other amyloids (31, 32), suggesting that it represents a minimal generic anti-amyloid LCP pharmacophore. Second, therapeutic efficacy requires charged side groups, because carboxylic acids and acetic acids (but not aldehydes or ketones) conferred effectiveness. Third, compounds comprising five thiophene or selenophene rings are only effective when bearing anionic side groups linked to the terminal thiophene rings. LIN5001 featured biterminal carboxyl residues, whose removal, or replacement with aldehydes or ketones, greatly reduced its efficacy. Similarly, the biterminally carboxylated LIN5050 was therapeutic, whereas the nonfunctionalized homolog (LIN5051) was ineffective. The terminal carboxyl groups are also important for differentiating Aβ from tau aggregates by fluorescence spectroscopy (30–32), suggesting that they contribute to the binding of many diverse amyloids. Fourth, the periodicity of the anionic side groups controls the antiprion properties, with the most effective pattern of regioregular charges being ≈5 Å–10 Å–5 Å (as in LIN5044). In contrast, the sequence ≈10 Å–5 Å–10 Å (as in the LIN5044 isomer, LIN5001) led to reduced activity. Parallel β sheets of amyloids are spaced 4.8 Å apart, suggesting that LCPs form electrostatic bonds to complementary cationic side

**Fig. 4. Antiprion potency of lead compound LIN5044.** (**A**) Therapeutic administration of LIN5044 by continuous intracerebral (ic) infusion starting at 49 dpi prolonged the life of prion-infected *tg*a20 mice (*n* = 8) by 21.8% over vehicle (*n* = 6; *P* = 0.0018). Log-rank Mantel-Cox test was used for survival analyses. (**B**) Intraperitoneal injections of LIN5044 (3 times per week) also significantly increased the survival of RML6-infected *tg*a20 mice (+14.5%; *n* = 6) compared to vehicle (*n* = 4; *P* = 0.044). (**C**) Western blot analysis of brains from prion-infected *tg*a20 mice treated by intracerebral infusion of LIN5044 and vehicle-treated controls. LIN5044-treated animals showed a reduction in proteinase K–resistant PrP. (**D**) Same as (C) for RML6-infected *tg*a20 mice treated with intraperitoneal (ip) injections of LIN5044 or vehicle. (**E**) Treatment with LIN5044 extended the survival of mice expressing hamster prion protein (tg81) and infected with a 263K prion strain (*n* = 9; +13.1%; *P* = 0.0003) compared to vehicle treatment (*n* = 5). (**F**) Western blot analysis of proteinase K–digested samples from brain homogenates of 263K-inoculated tg81 mice treated with LIN5044 intraperitoneally (eight representative samples) compared to four representative samples from vehicle-treated controls. (**G**) Histopathological analysis of brain sections from RML6-infected *tg*a20 mice prophylactically treated with vehicle or LIN5044 and sacrificed at 63 dpi. Neuronal cell loss, spongiform changes [hematoxylin and eosin (H&E)], and astrocyte reactivity [glial fibrillary acidic protein (GFAP)] in CA1 of the hippocampus were consistently detected in vehicle-treated mice but were strongly reduced or absent in LIN5044-treated mice. Non-infected *tg*a20 mice did not show any changes in brain tissue. Scale bars, 200 μm, 20 μm, and 50 μm.
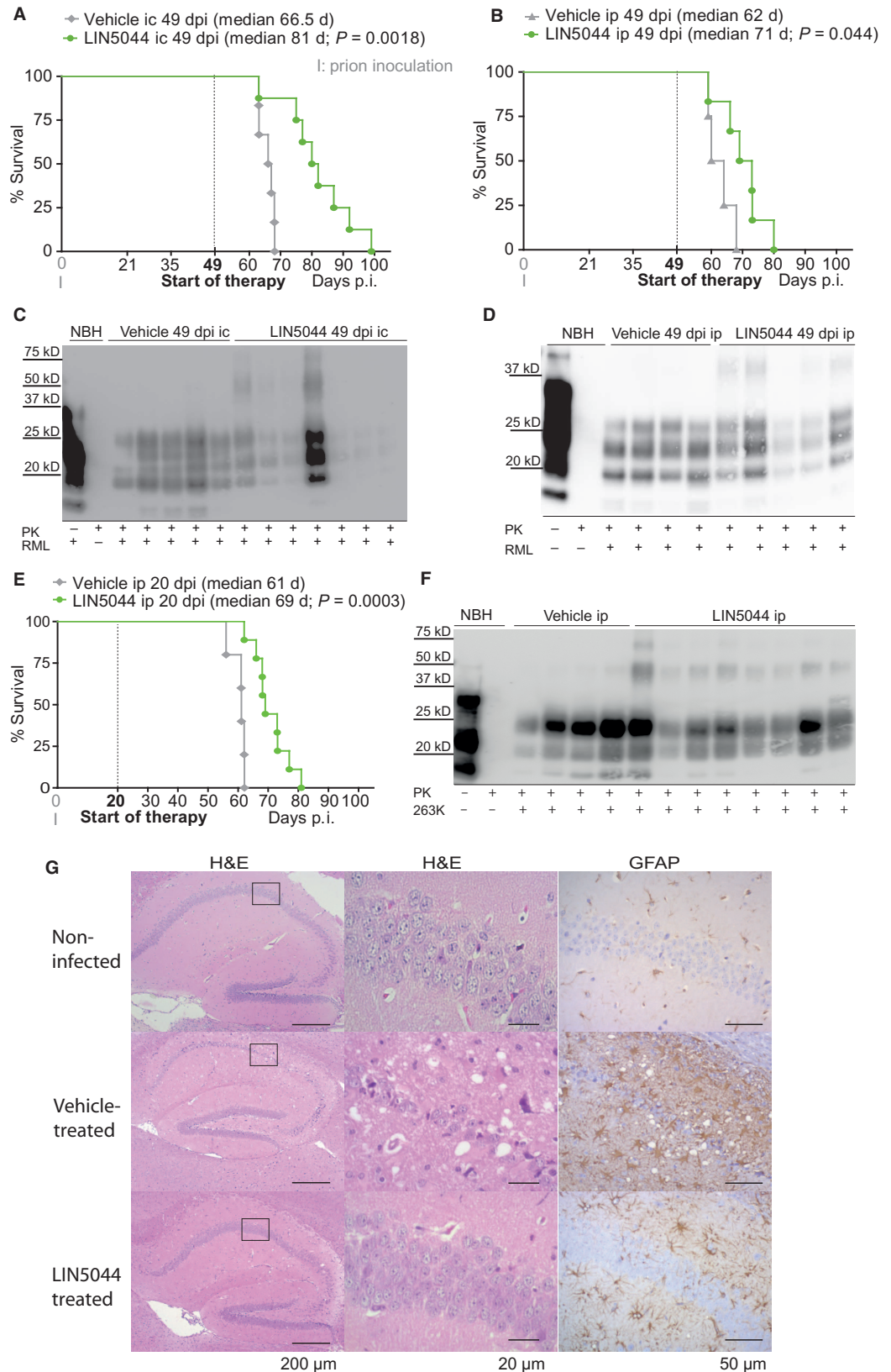
chains of amyloids. We verified this conjecture here experimentally for LIN5001 complexed to HET-s(218–289). Additionally, the regioregularity of the carboxyl groups influences the efficacy of LCPs, likely because of the structural constraints imposed by the β sheet stacks. Accordingly, the asymmetric LIN5043 was ineffective despite its pentathiophene backbone and biterminal carboxyl groups.

PrP$^{Sc}$ can appear as SDS-stable dimeric species (57). LCP treatment in vivo was associated with the enhanced appearance of proteinase K–resistant PrP$^{Sc}$ and SDS-stable high–molecular weight PrP oligomers, similar to co-incubation of LCPs with brain homogenates of prion-infected mice (Fig. 3I) (33). Furthermore, molecular dynamics simulations indicate that octameric β sheets acquired an enhanced structural stability upon binding to LIN5001. These findings support the conjecture that LCPs hyperstabilize PrP oligomers, thereby inhibiting the positive feedback loop in protein aggregation that generates new propagons through fragmentation or secondary nucleation (33). LCPs predicted to bind strongly by molecular dynamics simulations (LIN5044, LIN5045, and LIN7004) not only were the most efficient therapeutic molecules in vivo, but also resulted in reduced PrP$^{Sc}$ load and also in reduced numbers of PrP aggregates as measured by the misfolded protein assay. Reduced PrP deposition was confirmed by immunohistochemistry in brainstems of mice treated with LIN5044 and was associated with a conspicuous reduction in vacuolation and astrocytosis. In summary, (i) LCP treatment led to the appearance of protease- and SDS-resistant PrP oligomers, (ii) LCP treatment with the most active compounds reduced the amount of proteinase K–resistant PrP$^{Sc}$, (iii) molecular dynamics simulations suggested stabilization of oligomers, (iv) the misfolded protein assay highlighted a drastic reduction in PrP aggregates, (v) PrP deposition in histological sections was reduced, (vi) gradient ultracentrifugation showed reduced higher–molecular weight species, and (vii) seeding activity in vitro was reduced.

Fibril stabilization, and therefore reduced frangibility, might not be the only possible mode of action. The reduced seeding efficiency could also be due to slower nucleation, slower elongation, or inhibition of secondary nucleation. However, on the basis of the structural analyses, we deem it plausible that therapeutically efficacious LCPs bind and hyperstabilize small PrP$^{Sc}$ propagons, thereby reducing their infectivity. Furthermore, the increased survival of LIN5044-treated mice even when administered to preterminally scrapie-sick mice suggests that LCPs may attenuate PrP$^{Sc}$ toxicity. Because the latter cannot be directly quantified, this possibility must remain open. The findings described above validate the use of LCPs as candidate antiprion agents. LIN5044 was effective not only for prophylaxis but also during the symptomatic phase of the disease and, crucially, was active even after systemic administration, suggesting favorable pharmacodynamics/pharmacokinetics and brain penetration. Reassuringly, none of the monodisperse LCPs induced acute toxicity. The toxic heterodisperse LIN1001 was synthesized by random oxidative polymerization with FeCl₃, and its toxicity may be related to residual iron contaminants.

Strain selectivity often limits the practical usefulness of antiprion compounds (13, 14). However, LIN5044 was efficacious against both RML and 263K prions when administered to mice expressing mouse or hamster PrP$^{C}$ (52), raising hopes that LCPs may generically target multiple strains and perhaps even *PRNP* mutants.

There are some limitations to our study. HET-s is the only prion for which an atomic resolution structure was obtained. Several models for mammalian prions have been proposed, but no consensus has emerged yet, and there is no experimentally verified high-resolution structure.

Because HET-s and PrP$^{Sc}$ are very different molecules, one may wonder whether any HET-s–based rules for constructing LCP-based pharmacophores would be valid for PrP$^{Sc}$. In the instances explored here, the rules derived from the HET-s model predicted the biological activity of LCPs against mammalian prions. However, because this correlation was empirically derived, it may not retain validity for the entire chemical space of polythiophenes. Conversely, any deviations of future LCPs from the SAR relationships enunciated above may help in deriving structural information on the composition of mammalian prions.

Another potential limitation relates to the potential generalization of the above SAR rules to amyloids other than prions. Such generalization posits the existence of a common structural motif on the surface of chemically diverse amyloids. Because high-resolution structures are unavailable for most amyloids, it is currently impossible to test this assumption directly. Notwithstanding these limitations, our molecular dynamics simulations using octamers of the Aβ$_{10-20}$ peptide segment suggest the existence of a periodically repeated LIN7001 binding site consisting of regularly spaced cationic residues (KLVFF) in a parallel in-register β sheet, similar to PrP and HET-s. Hence, the SAR described here may be applicable to additional amyloids. This presumption, however, is currently speculative and may be superseded in the future, as the structural models of amyloids become refined.

In Alzheimer's disease, antibodies against Aβ can impressively reduce the plaque load in both mice (58, 59) and humans (60, 61) but have not yet been proven clinically efficacious (62, 63), possibly because large amyloid plaques are less relevant to disease progression than smaller aggregates. Accordingly, the amount and density of Aβ plaques correlate poorly with disease severity (64), whereas Aβ dimers from human brains are highly neurotoxic (65). In view of these findings, the preferential targeting of oligomers by LCPs may represent a therapeutic advantage. In conclusion, an iterative cycle of chemical synthesis, in vivo studies, solid-state NMR, and molecular dynamics simulations has identified LCPs as promising antiprion compounds (fig. S15). This cycle may be used for the discovery and optimization of further compounds with improved properties, thereby expanding the toolbox of therapeutic interventions against prion diseases and other proteinopathies.

## MATERIALS AND METHODS

### Study design

The purpose of this study was to evaluate the therapeutic potential of LCPs in a mouse model of prion disease (fig. S15). We selected the most efficient compound and chemically modified the backbone and the side chain to define the structure needed for therapeutic activity. Further, LCPs binding to the fungal HET-s model fibrils were obtained using solid-state NMR. We then performed molecular dynamics to calculate the free binding energies of newly designed LCPs to model fibrils. Finally, LCPs with high and low free binding energies were tested for their therapeutic efficiency in prion-infected mice, and a compound with enhanced prophylactic and therapeutic properties was found. The experiment was performed with age- and sex-matched randomly assigned mice, blinded to the experimenters. Mice were sacrificed at the terminal stage of the disease.

### Mice and prion inoculations

Wild-type CD1 and PrP-overexpressing mice [*tga20* (35)] were inoculated into the left hemisphere with 30 μl of RML6 brain homogenate.

The concentration was 0.001 and 0.1%, corresponding to $3 \times 10^3$ and $3 \times 10^5$ LD$_{50}$ (0.036 and 3.6 μg of total brain homogenate, respectively). Mice overexpressing hamster PrP$^C$ (tg81) (52) were injected in the left hemisphere with 30 μl of 263K (53) at a concentration of 0.1%. Mice were monitored in the presymptomatic phase every second day and in the clinical phase, on a daily basis. Scrapie was diagnosed according to clinical criteria including ataxia, kyphosis, tail rigidity, and hind leg paralysis. Mice were sacrificed at the terminal stage of the disease. All operated mice were kept in single cages and maintained under highly hygienic conditions. Mouse experiments were performed under licenses 130/2008, 41/2012, and 90/2013, and according to the regulations of the Veterinary Office of the Canton Zürich.

Organs for further study were taken as follows: the left sagittal half of the brain was fixed in 2% paraformaldehyde for immunohistochemistry. The cerebellum and the forebrain were separated from the other half of the brain. The remaining forebrain and cerebellar tissues were snap-frozen and stored for further biochemical analysis.

### Rotarod assay

To assess the initial clinical signs in prion-infected mice in an observer-independent manner, rotarod measurements that assess motor coordination and balance were performed. For the habituation phase, the mice were placed on the rotating drum (4 rpm) for three sessions, lasting 1 min each with 10 min between each session. After an interval of 15 min, the test phase was started that consisted of four trials separated by 15-min intervals. Each session lasted up to 300 s, whereas the rod accelerated from 5 to 40 rpm. Latency to fall was determined as the time point when the mouse was no longer able to run on the accelerating rod and either slipped from the drum or passively rotated with the rod. The experimenter was blinded to the treatment of the mice. The sessions were always performed at the same time of the day (10:00 a.m. to 12:00 p.m.).

### Synthesis of LCPs

The syntheses of LIN1001, LIN4003, LIN5001, LIN5002, LIN 5043, LIN5050, LIN5050, LIN7001, and LIN7002 have been described previously (30–32, 66). The syntheses of LIN4027, LIN5029, LIN5032, LIN5043, LIN5044, LIN5045, and LIN7004 are described in detail below.

**General procedures.** NMR spectra were recorded on a Varian 300 instrument or a Varian 500 instrument (Varian Inc.) operating at 300 or 500 MHz for $^1$H and 75.4 or 125 MHz for $^{13}$C, using the residual solvent signal as reference. Infrared (IR) spectra were acquired on a PerkinElmer Spectrum 1000 using KBr pellets. Chemicals and solvents were obtained from commercial sources and used as received. Thin-layer chromatography was carried out on Merck precoated 60 F254 plates using ultraviolet light (λ = 254 and 366 nm) and charring with ethanol/sulfuric acid/p-anisaldehyde/acetic acid 90:3:2:1 for visualization. Column chromatography was carried out on silica gel Merck 60 (40 to 63 μm).

*General procedure for Suzuki coupling.* PEPPSI-IPr (5 mol %) was added to a mixture of the bromothiophene/selenophene derivatives (1 to 2 equiv), K$_2$CO$_3$ (3 equiv per bromine), the desired boronic acid or pinacol esters (1 to 2 equiv per bromine) in 1,4-dioxane/methanol (8:2, 8 ml/mmol, degassed). The mixture was heated to 70°C for 20 min, cooled to room temperature, adjusted to pH 4 by 1 M HCl, extracted with dichloromethane (DCM) (3 × 30 ml/mmol), and washed with water (3× 30 ml/mmol) and brine (30 ml). The combined organic phases were dried over MgSO$_4$, and the crude product was either subjected to column chromatography or treated with appropriate solvent to give desired products.

*General procedure for bromination.* A solution of N-bromosuccinimide (1 or 2 equiv) in N,N′-dimethylformamide (DMF) (3 ml/mmol) was added dropwise to the desired thiophene derivative in DMF (2 ml/mmol) at 0°C. The mixture was allowed to reach room temperature overnight for 16 hours. Water was added, and the product was extracted with DCM (3× 30 ml/mmol). The combined organic phases were washed with water (3 × 30 ml/mmol), then brine (30 ml), dried over MgSO$_4$, and the solvent was evaporated under reduced pressure.

*General procedure for hydrolysis of methyl esters.* NaOH (1 M, 1.5 equiv per ester) was added to a solution of the oligothiophene/selenophene in 1,4-dioxane/H$_2$O (4:1, 7 ml/mmol) and heated to 60°C. The solution was stirred until precipitation, whereupon water was added and the solution was lyophilized.

### LIN5044

Compound **4** was synthesized as reported (67). The methyl ester protected product **7** was synthesized from compounds **4** and **6** (Sigma-Aldrich) according to the general procedure for Suzuki coupling (fig. S16A). By applying the general procedure for hydrolysis of methyl esters, **LIN5044** was rendered as a red solid.

IR (neat) 1572, 1453, 1391, 1379, 1319, 1255, 984, 881, 826, 801, 784, 772 cm$^{-1}$. $^1$H NMR (500 MHz, D$_2$O) δ 7.45 (d, J = 3.6 Hz, 1H), 7.15 (s, 1H), 7.06 (d, J = 3.6 Hz, 1H), 7.04 (s, 1H), 3.64 (s, 2H). $^{13}$C NMR (126 MHz, D$_2$O) δ 179.2, 169.6, 140.0, 139.7, 135.5, 135.1, 134.8, 131.3, 130.8, 128.1, 125.8, 124.7, 38.1.

### LIN7004

Compounds **4** and **8** were synthesized as reported (67). The methyl ester protected product **9** was synthesized from compounds **4** and **8** according to the general procedure for Suzuki coupling (fig. S16A). By applying the general procedure for hydrolysis of methyl esters, **LIN7004** was rendered as a red solid.

IR (neat) 1558, 1457, 1431, 1379, 1267, 986, 906, 879, 802, 773 cm$^{-1}$. $^1$H NMR (500 MHz, D$_2$O) δ 7.41 (d, J = 3.4 Hz, 1H), 7.31 (s, 1H), 7.01 (m, 2H), 3.63 (s, 2H). $^{13}$C NMR (126 MHz, D$_2$O) δ 179.1, 169.5, 141.9, 139.7, 139.6, 137.0, 135.0, 134.8, 131.5, 131.1, 130.9, 128.9, 127.8, 125.6, 38.3.

### LIN4027

Compound **11** was synthesized as reported previously (68). The methyl ester protected product **12** was synthesized from compounds **10** (Sigma-Aldrich) and **11** according to the general procedure for Suzuki coupling (fig. S16B). By applying the general procedure for hydrolysis of methyl esters, **LIN4027** was rendered as a red solid.

IR (neat) 1576, 1405, 1351, 1282, 981, 881, 822, 794, 777 cm$^{-1}$. $^1$H NMR (500 MHz, D$_2$O) δ 7.96 (d, J = 16.1 Hz, 1H), 7.36 (s, 1H), 7.20 to 7.04 (m, 2H), 6.28 (d, J = 16.1 Hz, 1H). $^{13}$C NMR (126 MHz, D$_2$O) δ 175.8, 169.3, 139.6, 137.8, 137.6, 136.4, 135.2, 133.6, 126.3, 125.9, 124.9, 122.6.

### LIN5045

Compounds **13** and **14** were synthesized as reported (67), and dimer **15** was synthesized from compounds **13** and **14** according to the general procedure for Suzuki coupling (fig. S16C). Compound **16** was generated from compound **15** by the general procedure for bromination. The methyl ester protected product **17** was synthesized from compounds **6** (purchased) and **16** according to the general procedure for Suzuki coupling. By applying the general procedure hydrolysis of methyl esters, **LIN5045** was rendered as a red solid.

IR (neat) 1576, 1389, 1281, 1155, 986, 918, 880, 833, 789 cm$^{-1}$. $^1$H NMR (500 MHz, D$_2$O) δ 7.23 (s, 1H), 7.18 (s, 1H), 7.09 (d, $J$ = 3.6 Hz, 1H), 6.94 (d, $J$ = 3.6 Hz, 1H), 3.75 (s, 2H), 3.68 (s, 2H). $^{13}$C NMR (126 MHz, D$_2$O) δ 179.4, 179.0, 139.2, 135.2, 134.0, 133.6, 133.5, 131.5, 130.1, 127.8, 126.8, 125.4, 124.5, 38.5, 38.0.

### LIN5029

The methyl ester protected product was synthesized from dibrominated thiophene trimer **18** (*30, 31*) using compound **19** (Sigma-Aldrich) according to the general procedure for Suzuki coupling (fig. S16D). During workup, the methyl ester protected product precipitated and was washed thoroughly with warm dioxane and added to a solution of dioxane/NaOH (1 M, aqueous), then heated at 75°C until everything dissolved. Acidification by HCl (1 M, aqueous) resulted in precipitation of the deprotected neutral product, which was washed with water and dried and dissolved in NaOH (1.5 equiv per carboxylic acid) to give **LIN5029** (1.05 g, 83%) as a red solid.

$^1$H NMR [300 MHz, dimethyl sulfoxide (DMSO)–d6] δ 7.85 (d, $J$ = 4.0 Hz, 2H), 7.46 (s, 2H), 7.40 (d, $J$ = 4.0 Hz, 2H), 7.30 (s, 2H), 3.75 (s, 4H), 2.49 (s, 6H); $^{13}$C NMR (75 MHz, DMSO-d6) δ 190.3, 171.4, 143.4, 142.4, 135.1, 134.6, 133.4, 133.3, 132.3, 130.3, 127.7, 125.3, 34.7, 26.3.

### Compound 21

The methyl ester protected compound **21** was first synthesized from dibrominated thiophene trimer **18** (*30, 31*) using compound **20** (Sigma-Aldrich) according to the general procedure for Suzuki coupling (fig. S16E). Purification by flash column chromatography (toluene/ethyl acetate, 6:1) and subsequent recrystallization from methylene chloride and methanol gave **21** (0.84 g, 75%) as a red solid.

$^1$H NMR (300 MHz, DMSO-d6) δ 9.90 (s, 2H), 8.00 (d, $J$ = 3.9 Hz, 2H), 7.57 (s, 2H), 7.56 (d, $J$ = 4.0 Hz, 2H), 7.36 (s, 2H), 3.90 (s, 4H), 3.68 (s, 6H); $^{13}$C NMR (75 MHz, DMSO-d6) δ 183.9, 170.4, 144.3, 141.7, 139.2, 134.6, 133.4, 133.1, 132.6, 130.8, 128.1, 125.7, 52.1, 34.1.

### LIN5032

Compound **21** (0.50 g, 0.816 mmol) was dissolved in dioxane (5 ml), and NaOH (1 M, aqueous, 2.45 ml) was added. The solution was stirred until precipitation, whereupon water (5 ml) was added and the solution was lyophilized to quantitatively render **LIN5032** as a red solid.

$^1$H NMR (300 MHz, DMSO-d6) δ 9.88 (s, 2H), 7.97 (d, $J$ = 3.9 Hz, 2H), 7.54 (s, 2H), 7.51 (d, $J$ = 4.0 Hz, 2H), 7.36 (s, 2H), 3.75 (s, 4H); $^{13}$C NMR (75 MHz, DMSO-d6) δ 35.4, 125.4, 127.7, 131.1, 132.8, 134.1, 134.7, 139.1, 141.4, 144.6, 171.6, 183.7.

### Preparation of LCP stock solutions

The synthesis of the different LCPs has been described elsewhere (*66*). Stock solutions of lyophilized LCPs were prepared at a concentration of 4 mg/ml in PBS and stored at 4°C, protected from light.

### Treatment of mice with LCPs

For the intracerebral treatment series, an osmotic pump (ALZET Model 2006; 0.15 μl/hour) was filled 48 hours before surgery with a stock solution (4 mg/ml) of the compounds or PBS as control and kept in PBS at 37°C or PBS as control. CD1 and *tga20* mice were anesthetized with isoflurane and placed in a motorized stereotaxic frame controlled by a software with a 3D brain map (NeuroStar), allowing for real-time monitoring of intraventricular infusion cannula (Alzet Brain Infusion Kit 3) placement. The skull was exposed by cutting along the midline, a small hole was drilled using a surgical drill, and a cannula was placed at the following coordinates from bregma: anteroposterior, −0.22 mm; mediolateral, 0.9 mm; and dorsoventral, 2.5 mm. The cannula, connected through a tube with the osmotic pump embedded in the subcutaneous tissue of the mice, was fixed to the skull with glue (AdheSE One F VivaPen Refill and Heraeus Kulzer Flowline). During and 12 hours after intervention, mice were treated with subcutaneous injections of Temgesic (Buprenorphin; 0.1 mg/kg), Finadyne (Flunixin; 5 mg/kg), and glucose 5% (20 μl/kg) to alleviate postoperative complications. At the first postoperative day, mice received Finadyne (2.5 mg/kg, two times per day) subcutaneously. Drinking water was supplemented with 2 ml of Borgal (trimethoprim/sulfadoxine) 24% and 30 g of sugar per liter for 1 week after surgery. The pump change was performed at 42 days after implantation. After skin incision, the old pump was replaced by a new one. Apart from the first LCP mix series, where only one pump change was performed, the pumps were changed every 42 days until the mice were terminal.

Prophylactic treatment was started 7 days before intracerebral injection of RML6 prions. LCP mix–treated *tga20* and CD1 mice in the first set of experiments were inoculated intracerebrally with RML6 prions (36 pg of total brain homogenate in 30 μl, corresponding to 3 × 10$^3$ LD$_{50}$ units). For all the other experiments, we used a 100-times higher RML6-prion titer corresponding to 3 × 10$^5$ LD$_{50}$ units (3.6 μg of total brain homogenate in 30 μl).

For the therapeutic LIN5044 experiments, the prion-infected *tga20* mice were randomly assigned to one of the following treatment arms: LIN5044 intraventricularly (3.3 mg/kg per week), vehicle intracerebrally, LIN5044 intraperitoneally (400 μg in 100 μl of PBS, three times weekly), or vehicle intraperitoneally.

### Preparation of mouse brain homogenates

Brain homogenates of RML6-infected or non-infected *tga20* mice were prepared in 0.32 M sucrose in PBS at a concentration of 20% (w/v) by two runs in a Precellys tissue homogenizer with cooling on ice between each run. Protein concentrations of RML6 or CD1 brain homogenates were determined by the bicinchoninic acid assay (Pierce).

### Western blot analyses

PrP$^{Sc}$ was detected by limited proteolysis with proteinase K (Roche) and analyzed by Western blotting. Samples were adjusted to 20 μg of protein in 20 μl and digested with proteinase K (25 μg/ml) in digestion buffer [0.5% (w/v) sodium deoxycholate and 0.5% (v/v) NP-40 in PBS] for 30 min at 37°C on the thermoshaker. These conditions allowed for the specific detection of PrP$^{Sc}$. Proteinase K digestion was terminated by adding 7 μl of 4× loading buffer (NuPAGE, Invitrogen) and boiling samples at 95°C for 5 min. Ten microliters of the samples was separated on a 12% bis-tris SDS polyacrylamide gel (NuPAGE, Invitrogen) and blotted onto a nitrocellulose membrane. Membranes were blocked for 1 hour at room temperature with 5% (w/v) Top-Block (Fluka) in tris-buffered saline supplemented with Tween 20 [150 mM NaCl, 10 mM tris-HCl, 0.05% Tween 20 (v/v)] and incubated with POM1 mouse immunoglobulin G1 (IgG1) antibody to PrP$^C$ (anti-PrP$^C$) (200 ng/ml) as primary antibody. Horseradish peroxidase–conjugated rabbit anti–mouse IgG1 (1:10,000; Zymed) was used as a secondary antibody. The blots were developed using SuperSignal West Pico chemiluminescent substrate (Pierce) and detected in a LAS3000 system (Fuji).

## Atomistic simulations

We devised a minimal model of an LCP binding site on a prion fibril that, despite its simplicity, captures the main interactions at the atomic level of detail. The model consisted of eight 3-residue peptides (S-A-K) arranged in a parallel in-register β sheet. The initial coordinates were derived from the HET-s NMR structure (PDB code 2LBU), in which the docked Congo red lies within a groove that is perpendicular to the solenoid β sheet (48). The groove originates from parallel β strands of alternating $S^{227}$-$A^{228}$-$K^{229}$ and $S^{263}$-$V^{264}$-$E^{265}$ segments where the backbone atoms of the central residues (that is, $A^{228}$ and $V^{264}$) form the floor of the groove and the side chains of residues $S^{227}$/$S^{263}$ and $K^{229}$/$E^{265}$ represent the walls. To generate the initial parallel in-register β sheet arrangement of eight S-A-K peptides, residues $V^{264}$ and $E^{265}$ were mutated into Ala and Lys, respectively, using visual molecular dynamics (51). The peptide termini were neutralized, whereas the Lys side chains were considered charged. The LCPs were docked manually according to the binding mode of Congo red, that is, with each carboxylate group of the LCPs pointing toward the nearest Lys side chain nitrogen.

The structure of the parallel in-register β sheet (consisting of eight S-A-K peptides or other tripeptides) in the complex with the manually docked LCP was immersed in a cubic box of pre-equilibrated water molecules. The size of the box was chosen to have a minimal distance of 10 Å between the boundary and any atom of the protein. Water molecules within 2.4 Å of any heavy atom of the peptide or LCPs were removed. Sodium and chloride ions were added to compensate for the total charge of the β sheet–LCP system and to obtain a final ion concentration of 150 mM. All molecular dynamics simulations were carried out with GROMACS (69) using the CHARMM22 force field (70, 71) and the TIP3P model of water (71) (note that the CHARMM36 force field was not yet available when this project was started). The parameters of LCP were determined according to the general CHARMM force field (72, 73).

Periodic boundary conditions were applied, and electrostatic interactions were evaluated using the particle mesh Ewald summation method (74, 75). The van der Waals interactions were truncated at a cutoff of 10 Å. The temperature during the molecular dynamics simulations was kept constant (310 K) by the v-rescale algorithm (75), and the pressure was kept at 1 atm by the Berendsen algorithm (76). The linear constraint solver algorithm (77) was used to fix the covalent bonds involving hydrogen atoms, which afforded a time step of 2 fs.

The free energy profiles were calculated by the umbrella sampling protocol (78) as implemented in GROMACS. The non-hydrogen atoms of the peptides were restrained to the initial octameric β sheet structure with a harmonic potential of 10,000 kJ mol$^{-1}$ nm$^{-2}$. First, the LCP was pulled at a rate of 5 nm ns$^{-1}$ of the binding groove along the direction spanned by the center of mass of the octameric β sheet and the center of mass of the LCP. The umbrella sampling protocol consisted of a series of simulations along the unbinding pathway with a window size of 0.05 nm using a harmonic potential of 3000 kJ mol$^{-1}$ nm$^{-2}$ applied at the center of mass of the LCPs. The free energy profile over the reaction coordinate was constructed using the weighted histogram analysis method (79).

## Misfolded protein assay

Aggregated PrP was assessed by using the misfolded protein assay (33, 36–38). Sixty micrograms of total protein [brain homogenate prepared as 1% (w/v) in 0.32 M sucrose in PBS] from brain homogenates

in 60 μl of TBSTT [50 mM tris-HCl (pH 7.5)/137 mM NaCl/1% Tween 20/1% Triton X-100] was diluted 100-fold in TBSTT. One hundred microliters was then subjected to precipitation using magnetic beads coupled to the peptoid PSR1 (36) for 1 hour at 37°C under permanent agitation (750 rpm). Beads were washed and denatured with 0.1 N NaOH (pH 12.3). After neutralization [0.3 M NaH$_2$PO$_4$ (pH 4.3)], samples were placed on a magnet, and the supernatant was transferred to POM19 (80)–coated enzyme-linked immunosorbent assay plates. After incubation (1 hour at 37°C, 300 rpm), plates were washed, and alkaline phosphatase–conjugated POM2 (80) was added. After incubation with substrate [100 μl of Lumi-Phos Plus substrate (Lumigen)], plates were read in a luminometry reader (Luminoskan Ascent; Thermo Fisher Scientific).

## In vitro binding assay

The expression and purification of recombinant mouse rPrP (residues 23 to 231) were performed as described (81–83). rPrP fibrils were prepared by incubating the protein in 50 mM tris-HCl, 1 M GdnHCl, and 150 mM sodium chloride (pH 7.5) for 48 hours at 37°C and shaking at 600 rpm (84). The concentration of rPrP fibrils was based on the concentration of the monomeric rPrP. After fibrillation, the absence of nonfibrillated rPrP was determined by measuring the concentration of rPrP in the supernatant. Fibrils were washed three times with 50 mM tris-HCl (pH 7.5), and LCP binding to the fibrils was investigated by mixing increasing amounts of the various LCPs ranging from 0 to 1000 nM with rPrP fibrils of a final concentration of 5 μM in 50 mM tris-HCl (pH 7.5). Binding of the LCPs was then monitored by fluorescence emission at a fixed wavelength while scanning the excitation spectra of the LCPs between 360 and 520 nm using the Paradigm SpectraMax Plate Reader (Corning 96-well half area black flat bottom plates). The fixed emission wavelengths used for the different LCPs were 545 nm for LIN5001, LIN7002, and LIN5029, and 540 nm for all other LCPs. The ratio of the maximum excitation intensities (Exc$_{max}$) for bound and unbound LCPs were calculated and normalized. The Exc$_{max}$ values for bound LCPs were between 460 and 470 nm, except for LIN4027 and LIN4003, which were 435 and 410 nm, respectively. For unbound LCPs, Exc$_{max}$ values between 370 and 390 nm were used for the different LCPs, except for LIN7001 and LIN7004, where 415 and 425 nm, respectively, were used. For better distinction between the values of unbound and bound LIN5043, LIN5044, and LIN4045, the less well-pronounced Exc$_{max}$ at 385 and 390 nm, respectively, of the unbound LCPs were used as unbound Exc$_{max}$ values. Data were then fitted with a hyperbola function in GraphPad to obtain the apparent $K_d$ values. Measurements were performed in triplicates.

## Resistance of rPrP fibrils to proteolysis in the presence of LIN5044

rPrP fibrils were prepared as described above, washed with 50 mM tris-HCl (pH 7.4), and incubated in the absence and presence of 50 μM LIN5044 at 37°C for 60 min on a thermoshaker at 900 rpm. Forty microliters of nontreated and LIN5044-treated fibrils with a concentration of 0.1 mg/ml was incubated with 0.4 M GdmHCl for 1 hour at room temperature. Fibrils were diluted with 360 μl of 10 mM tris-HCl (pH 8.0), 150 mM NaCl, 0.5% NP-40, and 0.5% deoxycholate, and digested with proteinase K (0.05 mg/ml) for 60 min at 37°C. Proteinase K digestion was terminated by adding phenylmethylsulfonyl fluoride at a final concentration of 1.5 mM. Proteins were precipitated with four volumes of ice-cold acetone overnight and centrifuged at 16,000g for 1 hour. Forty microliters of lauryl dodecyl sulfate loading buffer diluted in

PBS was added. Samples were boiled at 95°C for 5 min before loading on an SDS–polyacrylamide gel electrophoresis (SDS-PAGE) (NuPAGE, Invitrogen). Eighteen microliters of proteinase K–digested fibrils and 5 μl of undigested fibrils were loaded onto each lane. Samples were then analyzed by Western blotting.

## Histological analysis

Formalin-fixed tissues were treated with concentrated formic acid for 60 min to inactivate prion infectivity. Postfixation in formalin was performed, and tissues were embedded in paraffin. Paraffin sections (2 μm) of brains were stained with H&E. Antibodies against GFAP (astrocyte-specific, 1:300; Dako) were applied and visualized using standard methods. After deparaffinization, sections were incubated for 6 min in 98% formic acid and washed in distilled water for 30 min. Sections were then heated to 100°C in a steamer in citrate buffer (pH 6.0) for 3 min and allowed to cool down to room temperature. Sections were incubated in Ventana buffer, and stains were performed on a NEXEX immunohistochemistry robot (Ventana Instruments) using an iVIEW DAB Detection Kit (Ventana). After incubation with protease 1 (Ventana) for 16 min, sections were incubated with anti-PrP SAF-84 (SPI-Bio, A03208, 1:200) for 32 min. Sections were counterstained with hematoxylin.

## NMR sample preparation

Uniformly labeled [$^{15}$N and $^{13}$C] and perdeuterated [$^{2}$D, $^{15}$N, and $^{13}$C] HET-s(218–289)$^{E265K}$ protein as well as wild-type HET-s(218–289) were recombinantly expressed, and fibrils were prepared as described previously (48, 85). NMR samples were prepared by staining fibrillized protein with a fivefold molar excess of LIN5001 in deionized water overnight and gently mixing at room temperature. Unbound dye was subsequently washed off by 10 cycles of centrifugation and resuspension in 10 ml of 50 mM tris-HCl (pH 7.4) (protonated samples for CSP) or pure D$_2$O (perdeuterated samples for PT). The supernatant after the last centrifugation was nearly colorless. Samples for CSP measurements were finally suspended using 50 mM tris-HCl buffer (pH 7.4) or D$_2$O, respectively. A reference sample without LCP was prepared from each batch of protein and treated identically at all times.

## NMR measurements

NMR spectra for CSP/PT were recorded at sample temperatures of 5° to 10°C on Bruker Avance II+/Avance III 600/850 spectrometers operating at static magnetic fields of 14.1/20.0 T using a Bruker 3.2-mm triple-resonance probe spinning at 13/19 kHz, respectively. PDSD spectra with 50-ms mixing time were recorded with an initial cross-polarization step of 0.5 ms with radio frequency fields of 92 kHz on protons and 81 kHz on carbons. The maximal acquisition times were 13 ms in the indirect and 16 ms in the direct dimension. PT spectra used dipolar recoupling enhanced by amplitude modulation (DREAM) mixing and were recorded with an initial cross-polarization step of 9.0 ms, optimized for the long-distance transfer from the LCP protons to the protein $^{13}$C spin, with radio frequency fields of 86 kHz on protons and 70 kHz on carbons, and 4-ms DREAM mixing time. The maximal acquisition times were 5 ms in the indirect and 15 ms in the direct dimension. The total measurement times were 1 day for the PDSD spectra and 2.5 days for the PT spectra. Processing and analysis of the spectra were performed as described in (48).

## Model building

Docking was performed in HADDOCK (49) as described (48). The E265K point-mutated fibril of HET-s(218–289) was generated from PDB 2RNM using PyMOL (the PyMOL Molecular Graphics System, version 1.2r3pre; Schrödinger, LLC) (http://pymol.sourceforge.net/faq.html). PT and CSP data were translated into unambiguous 4.0-Å upper distance restraints between aliphatic atoms in the core region of the protein and any atom of LIN5001 (table S2). For the terminal lysine side-chain atoms (CD and CE) that displayed the strongest CSPs, these limits were reduced to 3.0 Å and implemented explicitly to the carboxyl atoms of LIN5001 identified in the initial docking, namely, K$^{229}$/K$^{229}$/K$^{265}$/K$^{265}$. It should, however, be noted that the carboxyl residue of LIN5001 can electrostatically interact with two adjacent lysines (K$^{229}$ and K$^{265}$) simultaneously. A 10 Å/10 Å/10 Å pattern as it exists on wild-type HET-s cannot be fulfilled by LIN5001. One thousand structures were calculated using rigid-body docking, the best 200 were chosen for semiflexible docking and subsequent explicit solvent refinement. The docking converged to a single cluster. The complexes were favorable in terms of van der Waals electrostatic energy ($-90.1 \pm 18.4$ kcal/mol) and buried surface area ($779.2 \pm 23$ Å$^2$).

## Seeding fibril conversion assay

Natively folded His-tagged rPrP (mouse PrP23-230) was purified as previously described (86), and a final concentration of 5 μM PrP in buffer F [50 mM phosphate (pH 7.4), 100 mM NaCl, 50 mM KCl] was used for all experiments. Brain homogenates from experimental animals and Prnp$^{-/-}$ animals (87) were prepared as previously described for Western blots. The following sample groups were selected for the conversion assay: vehicle-treated sacrificed at 63 days ($n = 3$) and at the terminal stage ($n = 2$), LIN5044-treated sacrificed at 63 days ($n = 3$) and at the terminal stage ($n = 2$), LIN5043-treated at the terminal stage ($n = 2$), and LIN5001-treated at the terminal stage ($n = 2$). Brain homogenate from a pool of Prnp$^{-/-}$ mice was used as negative control. The homogenates were diluted to 0.1% in buffer F, vortexed, and supplemented to experimental reactions at a final concentration of 0.01%. ThT was added to the sample at a final concentration of 2 μM. Fibrillation kinetics was monitored using a Tecan Safire$^2$ plate reader (88). In brief, 100 μl of samples was linearly shaken at 37°C, and ThT intensity at 480 nm (excitation, 440 nm) was monitored every 15 min during the time course of the experiment (96 hours). All samples were run in six replicates. Fibril conversion was defined by a ThT fluorescence threshold reaching >1000 arbitrary fluorescence intensity units, which was twice the intensity compared to initial conditions. Final fluorescence intensity was 10,000 ± 5000 for converted samples and 700 ± 300 for nonconverted samples after 96 hours.

## Density gradient centrifugation

A total amount of 400 μg of mouse brain homogenates was solubilized by adding 200 μl of solubilization buffer [50 mM Hepes (pH 7.4), 300 mM NaCl, 10 mM EDTA, 2 mM dithiothreitol (DTT), 4% (wt/vol) dodecyl-b-D-maltoside (Sigma)] and incubated for 45 min on ice. Next, 200-μl of sarkosyl (N-lauryl sarcosine; Fluka) was added to a final concentration of 2% (w/v), and the incubation continued for a further 30 min on ice. Four hundred microliters of the samples was loaded on a 3.6-ml continuous 5 to 20% (OptiPrep, Sigma), with a final concentration of 25 mM Hepes (pH 7.4), 150 mM NaCl, 2 mM EDTA, 1 mM DTT, and 0.5% sarkosyl. The gradients were centrifuged at 52,000 rpm for 90 min at 4°C (with a Discovery M150SE Micro-Ultracentrifuge and S52-ST swinging bucket). Fractions of 200 μl were collected, and 20 μl was analyzed on 12% bis-tris SDS polyacrylamide gel (NuPAGE, Invitrogen) followed by Western blotting as described above. For proteinase K digestion, 20 μl of sample was treated with proteinase K (20 μg/ml).

## Treatment of HET-s(218–289)$^{E265K}$ fibrils with LIN5044

Fifty micrograms of aggregated and HET-s(218–289)$^{E265K}$ was incubated without and with 1 μM LIN5044 in 100 mM tris-HCl, 150 mM NaCl (pH 8.0) for 1 hour at 37°C under shaking (600 rpm) in a volume of 50 μl. After the incubation, one volume of SDS-PAGE loading buffer was added, and samples were heated at 100°C for 5 min. Ten microliters of each reaction was analyzed by SDS-PAGE followed by silver staining.

## Statistical analyses

Survival times were analyzed by Kaplan-Meier survival curves using a log-rank Mantel-Cox test for curve comparisons. One-way ANOVA with Dunnett's posttest was used for statistical analysis of experiments involving the comparison of three or more samples. Paired Student's *t* test was used for comparing two samples. Results are displayed as the average of replicates ± SEM.

## SUPPLEMENTARY MATERIALS

www.sciencetranslationalmedicine.org/cgi/content/full/7/299/299ra123/DC1
Fig. S1. Western blot analyses of samples from brain homogenates of RML6-infected *tga20* mice treated with the LCP mix or the single compounds.
Fig. S2. Histopathological analysis of brain sections from *tga20* mice treated with vehicle, LIN5032, LIN5001, or LIN5050.
Fig. S3. Western blots of fractions after density gradient ultracentrifugation for two further biological replicates of brain homogenates of non-infected, prion-infected vehicle-, LIN5002-, and LIN5001-treated mice using a 10 to 40% OptiPrep gradient.
Fig. S4. Western blots of fractions after density gradient ultracentrifugation of brain homogenates of non-infected, prion-infected vehicle-, LIN5002-, and LIN5001-treated mice using a 5 to 20% OptiPrep gradient.
Fig. S5. Aliphatic region of solid-state NMR spectra of HET-s(218–289).
Fig. S6. Free energy profiles of binding of newly designed LCPs.
Fig. S7. The structural stability of in-register parallel β sheet oligomers consisting of eight copies of the 177–216 segment of the mouse prion protein in the absence and presence of LIN5001.
Fig. S8. Structural stability of in-register parallel β sheet oligomers consisting of eight copies of the segment of Aβ$_{10-20}$ in the absence and presence of LIN7001.
Fig. S9. Fluorescence excitation binding curves of different LCPs to recombinant rPrP fibrils as a function of LCP concentration.
Fig. S10. Molecular structures of additional LCPs used in the in silico approach, but not for in vivo testing.
Fig. S11. Silver-stained SDS-PAGE of HET-s(218–289)$^{E265K}$ incubated with LIN5044 (1 μg/ml).
Fig. S12. Brain histology of terminal prion-infected *tga20* mice treated with LIN5044, LIN5043, or vehicle compared to non-infected, untreated *tga20* mice.
Fig. S13. Rotarod and Western blot analysis.
Fig. S14. In vitro seeding efficiency for LCP- and vehicle-treated mice studied by the ThT fluorescence fibril conversion assay of rPrP.
Fig. S15. Flow chart of the iterative cycle of chemical synthesis, in vivo studies, solid-state NMR, and molecular dynamics simulations for the discovery of antiprion drugs.
Fig. S16. Schemes of the synthesis of the different LCPs.
Table S1. Results of the in vivo experiments.
Table S2. NMR-derived distance restraints for the HADDOCK model of LIN5001 in complex with the E265K point mutant of HET-s(218–289).
Table S3. Binding affinities of selected LCPs to rPrP in vitro.
Movie S1. LIN5001 bound to fibrils consisting of T-A-K.
Movie S2. LIN5001 pulled out of the binding with T-A-K.
Movie S3. Molecular dynamics simulation of the octameric hendecapeptide segment Aβ$_{10-20}$ in the apo form.
Movie S4. Molecular dynamics simulation of the octameric hendecapeptide segment Aβ$_{10-20}$ in the presence of LIN7001.

## REFERENCES AND NOTES

1. S. B. Prusiner, Novel proteinaceous infectious particles cause scrapie. *Science* **216**, 136–144 (1982).
2. A. Aguzzi, T. O'Connor, Protein aggregation diseases: Pathogenicity and therapeutic perspectives. *Nat. Rev. Drug Discov.* **9**, 237–248 (2010).
3. B. S. Appleby, C. G. Lyketsos, Rapidly progressive dementias and the treatment of human prion diseases. *Expert Opin. Pharmacother.* **12**, 1–12 (2011).
4. C. Weissmann, A. Aguzzi, Approaches to therapy of prion diseases. *Annu. Rev. Med.* **56**, 321–344 (2005).
5. J. A. Moreno, M. Halliday, C. Molloy, H. Radford, N. Verity, J. M. Axten, C. A. Ortori, A. E. Willis, P. M. Fischer, D. A. Barrett, G. R. Mallucci, Oral treatment targeting the unfolded protein response prevents neurodegeneration and clinical disease in prion-infected mice. *Sci. Transl. Med.* **5**, 206ra138 (2013).
6. M. Pietri, C. Dakowski, S. Hannaoui, A. Alleaume-Butaux, J. Hernandez-Rapp, A. Ragagnin, S. Mouillet-Richard, S. Haik, Y. Bailly, J. M. Peyrin, J. M. Launay, O. Kellermann, B. Schneider, PDK1 decreases TACE-mediated α-secretase activity and promotes disease progression in prion and Alzheimer's diseases. *Nat. Med.* **19**, 1124–1131 (2013).
7. F. L. Heppner, C. Musahl, I. Arrighi, M. A. Klein, T. Rülicke, B. Oesch, R. M. Zinkernagel, U. Kalinke, A. Aguzzi, Prevention of scrapie pathogenesis by transgenic expression of anti-prion protein antibodies. *Science* **294**, 178–182 (2001).
8. M. Polymenidou, F. L. Heppner, E. C. Pellicioli, E. Urich, G. Miele, N. Braun, F. Wopfner, H. M. Schätzl, B. Becher, A. Aguzzi, Humoral immune response to native eukaryotic prion protein correlates with anti-prion protection. *Proc. Natl. Acad. Sci. U.S.A.* **101**, 14670–14676 (2004).
9. L. Solforosi, J. R. Criado, D. B. McGavern, S. Wirz, M. Sánchez-Alavez, S. Sugama, L. A. DeGiorgio, B. T. Volpe, E. Wiseman, G. Abalos, E. Masliah, D. Gilden, M. B. Oldstone, B. Conti, R. A. Williamson, Cross-linking cellular prion protein triggers neuronal apoptosis in vivo. *Science* **303**, 1514–1516 (2004).
10. T. Sonati, R. R. Reimann, J. Falsig, P. K. Baral, T. O'Connor, S. Hornemann, S. Yaganoglu, B. Li, U. S. Herrmann, B. Wieland, M. Swayampakula, M. H. Rahman, D. Das, N. Kav, R. Riek, P. P. Liberski, M. N. James, A. Aguzzi, The toxicity of antiprion antibodies is mediated by the flexible tail of the prion protein. *Nature* **501**, 102–106 (2013).
11. S. Supattapone, J. R. Piro, J. R. Rees, Complex polyamines: Unique prion disaggregating compounds. *CNS Neurol. Disord. Drug Targets* **8**, 323–328 (2009).
12. D. B. Berry, D. Lu, M. Geva, J. C. Watts, S. Bhardwaj, A. Oehler, A. R. Renslo, S. J. DeArmond, S. B. Prusiner, K. Giles, Drug resistance confounding prion therapeutics. *Proc. Natl. Acad. Sci. U.S.A.* **110**, E4160–E4169 (2013).
13. Y. Kawasaki, K. Kawagoe, C. J. Chen, K. Teruya, Y. Sakasegawa, K. Doh-ura, Orally administered amyloidophilic compound is effective in prolonging the incubation periods of animals cerebrally infected with prion diseases in a prion strain-dependent manner. *J. Virol.* **81**, 12889–12898 (2007).
14. D. Lu, K. Giles, Z. Li, S. Rao, E. Dolghih, J. R. Gever, M. Geva, M. L. Elepano, A. Oehler, C. Bryant, A. R. Renslo, M. P. Jacobson, S. J. Dearmond, B. M. Silber, S. B. Prusiner, Biaryl amides and hydrazones as therapeutics for prion disease in transgenic mice. *J. Pharmacol. Exp. Ther.* **347**, 325–338 (2013).
15. J. Wagner, S. Ryazanov, A. Leonov, J. Levin, S. Shi, F. Schmidt, C. Prix, F. Pan-Montojo, U. Bertsch, G. Mitteregger-Kretzschmar, M. Geissen, M. Eiden, F. Leidel, T. Hirschberger, A. A. Deeg, J. J. Krauth, W. Zinth, P. Tavan, J. Pilger, M. Zweckstetter, T. Frank, M. Bähr, J. H. Weishaupt, M. Uhr, H. Urlaub, U. Teichmann, M. Samwer, K. Bötzel, M. Groschup, H. Kretzschmar, C. Griesinger, A. Giese, Anle138b: A novel oligomer modulator for disease-modifying therapy of neurodegenerative diseases such as prion and Parkinson's disease. *Acta Neuropathol.* **125**, 795–813 (2013).
16. K. Doh-ura, K. Ishikawa, I. Murakami-Kubo, K. Sasaki, S. Mohri, R. Race, T. Iwaki, Treatment of transmissible spongiform encephalopathy by intraventricular drug infusion in animal models. *J. Virol.* **78**, 4999–5006 (2004).
17. H. Honda, K. Sasaki, H. Minaki, K. Masui, S. O. Suzuki, K. Doh-Ura, T. Iwaki, Protease-resistant PrP and PrP oligomers in the brain in human prion diseases after intraventricular pentosan polysulfate infusion. *Neuropathology* **32**, 124–132 (2012).
18. K. Doh-Ura, T. Iwaki, B. Caughey, Lysosomotropic agents and cysteine protease inhibitors inhibit scrapie-associated prion protein accumulation. *J. Virol.* **74**, 4894–4897 (2000).
19. J. Collinge, M. Gorham, F. Hudson, A. Kennedy, G. Keogh, S. Pal, M. Rossor, P. Rudge, D. Siddique, M. Spyer, D. Thomas, S. Walker, T. Webb, S. Wroe, J. Darbyshire, Safety and efficacy of quinacrine in human prion disease (PRION-1 study): A patient-preference trial. *Lancet Neurol.* **8**, 334–344 (2009).
20. S. Ghaemmaghami, M. Ahn, P. Lessard, K. Giles, G. Legname, S. J. DeArmond, S. B. Prusiner, Continuous quinacrine treatment results in the formation of drug-resistant prions. *PLOS Pathog.* **5**, e1000673 (2009).
21. J. Bian, H. E. Kang, G. C. Telling, Quinacrine promotes replication and conformational mutation of chronic wasting disease prions. *Proc. Natl. Acad. Sci. U.S.A.* **111**, 6028–6033 (2014).
22. S. Haïk, G. Marcon, A. Mallet, M. Tettamanti, A. Welaratne, G. Giaccone, S. Azimi, V. Pietrini, J. R. Fabreguettes, D. Imperiale, P. Cesaro, C. Buffa, C. Aucan, U. Lucca, L. Peckeu, S. Suardi, C. Tranchant, I. Zerr, C. Houillier, V. Redaelli, H. Vespignani, A. Campanella, F. Sellal, A. Krasnianski, D. Seilhean, U. Heinemann, F. Sedel, M. Canovi, M. Gobbi, G. Di Fede, J. L. Laplanche, M. Pocchiari, M. Salmona, G. Forloni, J. P. Brandel, F. Tagliavini, Doxycycline in Creutzfeldt-Jakob disease: A phase 2, randomised, double-blind, placebo-controlled trial. *Lancet Neurol.* **13**, 150–158 (2014).

23. B. Cox, F. Ness, M. Tuite, Analysis of the generation and segregation of propagons: Entities that propagate the [PSI+] prion in yeast. *Genetics* **165**, 23–33 (2003).

24. T. P. Knowles, C. A. Waudby, G. L. Devlin, S. I. Cohen, A. Aguzzi, M. Vendruscolo, E. M. Terentjev, M. E. Welland, C. M. Dobson, An analytical solution to the kinetics of breakable filament assembly. *Science* **326**, 1533–1537 (2009).

25. A. Herland, K. P. Nilsson, J. D. Olsson, P. Hammarström, P. Konradsson, O. Inganäs, Synthesis of a regioregular zwitterionic conjugated oligoelectrolyte, usable as an optical probe for detection of amyloid fibril formation at acidic pH. *J. Am. Chem. Soc.* **127**, 2317–2323 (2005).

26. K. P. Nilsson, P. Hammarström, F. Ahlgren, A. Herland, E. A. Schnell, M. Lindgren, G. T. Westermark, O. Inganäs, Conjugated polyelectrolytes—Conformation-sensitive optical probes for staining and characterization of amyloid deposits. *Chembiochem* **7**, 1096–1104 (2006).

27. K. P. Nilsson, A. Herland, P. Hammarström, O. Inganäs, Conjugated polyelectrolytes: Conformation-sensitive optical probes for detection of amyloid fibril formation. *Biochemistry* **44**, 3718–3724 (2005).

28. K. P. Nilsson, K. Ikenberg, A. Aslund, S. Fransson, P. Konradsson, C. Röcken, H. Moch, A. Aguzzi, Structural typing of systemic amyloidoses by luminescent-conjugated polymer spectroscopy. *Am. J. Pathol.* **176**, 563–574 (2010).

29. C. J. Sigurdson, K. P. Nilsson, S. Hornemann, G. Manco, M. Polymenidou, P. Schwarz, M. Leclerc, P. Hammarström, K. Wüthrich, A. Aguzzi, Prion strain discrimination using luminescent conjugated polymers. *Nat. Methods* **4**, 1023–1030 (2007).

30. A. Aslund, C. J. Sigurdson, T. Klingstedt, S. Grathwohl, T. Bolmont, D. L. Dickstein, E. Glimsdal, S. Prokop, M. Lindgren, P. Konradsson, D. M. Holtzman, P. R. Hof, F. L. Heppner, S. Gandy, M. Jucker, A. Aguzzi, P. Hammarström, K. P. Nilsson, Novel pentameric thiophene derivatives for in vitro and in vivo optical imaging of a plethora of protein aggregates in cerebral amyloidoses. *ACS Chem. Biol.* **4**, 673–684 (2009).

31. T. Klingstedt, A. Aslund, R. A. Simon, L. B. Johansson, J. J. Mason, S. Nyström, P. Hammarström, K. P. Nilsson, Synthesis of a library of oligothiophenes and their utilization as fluorescent ligands for spectral assignment of protein aggregates. *Org. Biomol. Chem.* **9**, 8356–8370 (2011).

32. T. Klingstedt, H. Shirani, K. O. Åslund, N. J. Cairns, C. J. Sigurdson, M. Goedert, K. P. Nilsson, The structural basis for optimal performance of oligothiophene-based fluorescent amyloid ligands: Conformational flexibility is essential for spectral assignment of a diversity of protein aggregates. *Chemistry* **19**, 10179–10192 (2013).

33. I. Margalith, C. Suter, B. Ballmer, P. Schwarz, C. Tiberi, T. Sonati, J. Falsig, S. Nyström, P. Hammarström, A. Aslund, K. P. Nilsson, A. Yam, E. Whitters, S. Hornemann, A. Aguzzi, Polythiophenes inhibit prion propagation by stabilizing prion protein (PrP) aggregates. *J. Biol. Chem.* **287**, 18872–18887 (2012).

34. A. Ayrolles-Torro, T. Imberdis, J. Torrent, K. Toupet, I. V. Baskakov, G. Poncet-Montange, C. Gregoire, F. Roquet-Baneres, S. Lehmann, D. Rognan, M. Pugniere, J. M. Verdier, V. Perrier, Oligomeric-induced activity by thienyl pyrimidine compounds traps prion infectivity. *J. Neurosci.* **31**, 14882–14892 (2011).

35. M. Fischer, T. Rülicke, A. Raeber, A. Sailer, M. Moser, B. Oesch, S. Brandner, A. Aguzzi, C. Weissmann, Prion protein (PrP) with amino-proximal deletions restoring susceptibility of PrP knockout mice to scrapie. *EMBO J.* **15**, 1255–1264 (1996).

36. A. L. Lau, A. Y. Yam, M. M. Michelitsch, X. Wang, C. Gao, R. J. Goodson, R. Shimizu, G. Timoteo, J. Hall, A. Medina-Selby, D. Coit, C. McCoin, B. Phelps, P. Wu, C. Hu, D. Chien, D. Peretz, Characterization of prion protein (PrP)-derived peptides that discriminate full-length PrPSc from PrPC. *Proc. Natl. Acad. Sci. U.S.A.* **104**, 11551–11556 (2007).

37. M. Polymenidou, S. Prokop, H. H. Jung, E. Hewer, D. Peretz, R. Moos, M. Tolnay, A. Aguzzi, Atypical prion protein conformation in familial prion disease with PRNP P105T mutation. *Brain Pathol.* **21**, 209–214 (2011).

38. J. Falsig, T. Sonati, U. S. Herrmann, D. Saban, B. Li, K. Arroyo, B. Ballmer, P. Liberski, A. Aguzzi, Prion pathogenesis is faithfully reproduced in cerebellar organotypic slice cultures. *PLOS Pathog.* **8**, e1002985 (2012).

39. A. Y. Yam, X. Wang, C. M. Gao, M. D. Connolly, R. N. Zuckermann, T. Bleu, J. Hall, J. P. Fedynyshyn, S. Allauzen, D. Peretz, C. M. Salisbury, A universal method for detection of amyloidogenic misfolded proteins. *Biochemistry* **50**, 4322–4329 (2011).

40. A. Patra, M. Bendikov, Polyselenophenes. *J. Mater. Chem.* **20**, 422–433 (2010).

41. Y. H. Wijsboom, A. Patra, S. S. Zade, Y. Sheynin, M. Li, L. J. Shimon, M. Bendikov, Controlling rigidity and planarity in conjugated polymers: Poly(3,4-ethylenedithioselenophene). *Angew. Chem. Int. Ed. Engl.* **48**, 5443–5447 (2009).

42. F. Laferrière, P. Tixador, M. Moudjou, J. Chapuis, P. Sibille, L. Herzog, F. Reine, E. Jaumain, H. Laude, H. Rezaei, V. Béringue, Quaternary structure of pathological prion protein as a determining factor of strain-specific prion replication dynamics. *PLOS Pathog.* **9**, e1003702 (2013).

43. P. Tixador, L. Herzog, F. Reine, E. Jaumain, J. Chapuis, A. Le Dur, H. Laude, V. Béringue, The physical relationship between infectivity and prion protein aggregates is strain-dependent. *PLOS Pathog.* **6**, e1000859 (2010).

44. N. J. Cobb, F. D. Sönnichsen, H. McHaourab, W. K. Surewicz, Molecular architecture of human prion protein amyloid: A parallel, in-register β-structure. *Proc. Natl. Acad. Sci. U.S.A.* **104**, 18946–18951 (2007).

45. R. Diaz-Espinoza, C. Soto, High-resolution structure of infectious prion protein: The final frontier. *Nat. Struct. Mol. Biol.* **19**, 370–377 (2012).

46. B. R. Groveman, M. A. Dolan, L. M. Taubner, A. Kraus, R. B. Wickner, B. Caughey, Parallel in-register intermolecular β-sheet architectures for prion-seeded prion protein (PrP) amyloids. *J. Biol. Chem.* **289**, 24129–24142 (2014).

47. C. Wasmer, A. Lange, H. Van Melckebeke, A. B. Siemer, R. Riek, B. H. Meier, Amyloid fibrils of the HET-s(218–289) prion form a β solenoid with a triangular hydrophobic core. *Science* **319**, 1523–1526 (2008).

48. A. K. Schütz, A. Soragni, S. Hornemann, A. Aguzzi, M. Ernst, A. Böckmann, B. H. Meier, The amyloid–Congo red interface at atomic resolution. *Angew. Chem. Int. Ed. Engl.* **50**, 5956–5960 (2011).

49. S. J. de Vries, M. van Dijk, A. M. Bonvin, The HADDOCK web server for data-driven biomolecular docking. *Nat. Protoc.* **5**, 883–897 (2010).

50. J. Wigenius, M. R. Andersson, E. K. Esbjörner, F. Westerlund, Interactions between a luminescent conjugated polyelectrolyte and amyloid fibrils investigated with flow linear dichroism spectroscopy. *Biochem. Biophys. Res. Commun.* **408**, 115–119 (2011).

51. W. Humphrey, A. Dalke, K. Schulten, VMD: Visual molecular dynamics. *J. Mol. Graph.* **14**, 27–38 (1996).

52. M. Scott, D. Foster, C. Mirenda, D. Serban, F. Coufal, M. Wälchli, M. Torchia, D. Groth, G. Carlson, S. J. DeArmond, D. Westaway, S. B. Prusiner, Transgenic mice expressing hamster prion protein produce species-specific scrapie infectivity and amyloid plaques. *Cell* **59**, 847–857 (1989).

53. R. H. Kimberlin, C. A. Walker, Evidence that the transmission of one source of scrapie agent to hamsters involves separation of agent strains from a mixture. *J. Gen. Virol.* **39**, 487–496 (1978).

54. C. Govaerts, H. Wille, S. B. Prusiner, F. E. Cohen, Evidence for assembly of prions with left-handed β-helices into trimers. *Proc. Natl. Acad. Sci. U.S.A.* **101**, 8342–8347 (2004).

55. M. L. DeMarco, V. Daggett, From conversion to aggregation: Protofibril formation of the prion protein. *Proc. Natl. Acad. Sci. U.S.A.* **101**, 2293–2298 (2004).

56. R. Tycko, R. Savtchenko, V. G. Ostapchenko, N. Makarava, I. V. Baskakov, The α-helical C-terminal domain of full-length recombinant PrP converts to an in-register parallel β-sheet structure in PrP fibrils: Evidence from solid state nuclear magnetic resonance. *Biochemistry* **49**, 9488–9497 (2010).

57. S. A. Priola, B. Caughey, B. Wehrly, B. Chesebro, A 60-kDa prion protein (PrP) with properties of both the normal and scrapie-associated forms of PrP. *J. Biol. Chem.* **270**, 3299–3305 (1995).

58. F. Bard, R. Barbour, C. Cannon, R. Carretto, M. Fox, D. Games, T. Guido, K. Hoenow, K. Hu, K. Johnson-Wood, K. Khan, D. Kholodenko, C. Lee, M. Lee, R. Motter, M. Nguyen, A. Reed, D. Schenk, P. Tang, N. Vasquez, P. Seubert, T. Yednock, Epitope and isotype specificities of antibodies to β-amyloid peptide for protection against Alzheimer's disease–like neuropathology. *Proc. Natl. Acad. Sci. U.S.A.* **100**, 2023–2028 (2003).

59. F. Bard, C. Cannon, R. Barbour, R. L. Burke, D. Games, H. Grajeda, T. Guido, K. Hu, J. Huang, K. Johnson-Wood, K. Khan, D. Kholodenko, M. Lee, I. Lieberburg, R. Motter, M. Nguyen, F. Soriano, N. Vasquez, K. Weiss, B. Welch, P. Seubert, D. Schenk, T. Yednock, Peripherally administered antibodies against amyloid β-peptide enter the central nervous system and reduce pathology in a mouse model of Alzheimer disease. *Nat. Med.* **6**, 916–919 (2000).

60. J. O. Rinne, D. J. Brooks, M. N. Rossor, N. C. Fox, R. Bullock, W. E. Klunk, C. A. Mathis, K. Blennow, J. Barakos, A. A. Okello, S. Rodriguez Martinez de Liano, E. Liu, M. Koller, K. M. Gregg, D. Schenk, R. Black, M. Grundman, ¹¹C-PiB PET assessment of change in fibrillar amyloid-β load in patients with Alzheimer's disease treated with bapineuzumab: A phase 2, double-blind, placebo-controlled, ascending-dose study. *Lancet Neurol.* **9**, 363–372 (2010).

61. K. Blennow, H. Zetterberg, J. O. Rinne, S. Salloway, J. Wei, R. Black, M. Grundman, E. Liu; AAB-001 201/202 Investigators, Effect of immunotherapy with bapineuzumab on cerebrospinal fluid biomarker levels in patients with mild to moderate Alzheimer disease. *Arch. Neurol.* **69**, 1002–1010 (2012).

62. R. S. Doody, R. G. Thomas, M. Farlow, T. Iwatsubo, B. Vellas, S. Joffe, K. Kieburtz, R. Raman, X. Sun, P. S. Aisen, E. Siemers, H. Liu-Seifert, R. Mohs; Alzheimer's Disease Cooperative Study Steering Committee; Solanezumab Study Group, Phase 3 trials of solanezumab for mild-to-moderate Alzheimer's disease. *N. Engl. J. Med.* **370**, 311–321 (2014).

63. S. Salloway, R. Sperling, N. C. Fox, K. Blennow, W. Klunk, M. Raskind, M. Sabbagh, L. S. Honig, A. P. Porsteinsson, S. Ferris, M. Reichert, N. Ketter, B. Nejadnik, V. Guenzler, M. Miloslavsky, D. Wang, Y. Lu, J. Lull, I. C. Tudor, E. Liu, M. Grundman, E. Yuen, R. Black, H. R. Brashear; Bapineuzumab 301 and 302 Clinical Trial Investigator, Two phase 3 trials of bapineuzumab in mild-to-moderate Alzheimer's disease. *N. Engl. J. Med.* **370**, 322–333 (2014).

64. R. D. Terry, E. Masliah, D. P. Salmon, N. Butters, R. DeTeresa, R. Hill, L. A. Hansen, R. Katzman, Physical basis of cognitive alterations in Alzheimer's disease: Synapse loss is the major correlate of cognitive impairment. *Ann. Neurol.* **30**, 572–580 (1991).

65. G. M. Shankar, S. Li, T. H. Mehta, A. Garcia-Munoz, N. E. Shepardson, I. Smith, F. M. Brett, M. A. Farrell, M. J. Rowan, C. A. Lemere, C. M. Regan, D. M. Walsh, B. L. Sabatini, D. J. Selkoe, Amyloid-β protein dimers isolated directly from Alzheimer's brains impair synaptic plasticity and memory. *Nat. Med.* **14**, 837–842 (2008).

66. L. Ding, M. Jonforsen, L. S. Roman, M. Andersson, O. Inganäs, Photovoltaic cells with a conjugated poly electrolyte. *Synth. Met.* **110**, 133–140 (2000).

67. R. A. Simon, H. Shirani, K. O. Aslund, M. Bäck, V. Haroutunian, S. Gandy, K. P. Nilsson, Pentameric thiophene-based ligands that spectrally discriminate amyloid-β and tau aggregates display distinct solvatochromism and viscosity-induced spectral shifts. *Chemistry* **20**, 12537–12543 (2014).

68. T. Ueyama, S. Mochida, T. Fukutani, K. Hirano, T. Satoh, M. Miura, Ruthenium-catalyzed oxidative vinylation of heteroarene carboxylic acids with alkenes via regioselective C–H bond cleavage. *Org. Lett.* **13**, 706–708 (2011).

69. B. Hess, C. Kutzner, D. van der Spoel, E. Lindahl, GROMACS 4: Algorithms for highly efficient, load-balanced, and scalable molecular simulation. *J. Chem. Theory Comput.* **4**, 435–447 (2008).

70. A. D. MacKerell, D. Bashford, M. Bellott, R. L. Dunbrack, J. D. Evanseck, M. J. Field, S. Fischer, J. Gao, H. Guo, S. Ha, D. Joseph-McCarthy, L. Kuchnir, K. Kuczera, F. T. K. Lau, C. Mattos, S. Michnick, T. Ngo, D. T. Nguyen, B. Prodhom, W. E. Reiher, B. Roux, M. Schlenkrich, J. C. Smith, R. Stote, J. Straub, M. Watanabe, J. Wiórkiewicz-Kuczera, D. Yin, M. Karplus, All-atom empirical potential for molecular modeling and dynamics studies of proteins. *J. Phys. Chem. B* **102**, 3586–3616 (1998).

71. W. L. Jorgensen, J. Chandrasekhar, J. D. Madura, R. W. Impey, M. L. Klein, Comparison of simple potential functions for simulating liquid water. *J. Chem. Phys.* **79**, 926–935 (1983).

72. K. Vanommeslaeghe, E. Hatcher, C. Acharya, S. Kundu, S. Zhong, J. Shim, E. Darian, O. Guvench, P. Lopes, I. Vorobyov, A. D. MacKerell Jr., CHARMM general force field: A force field for drug-like molecules compatible with the CHARMM all-atom additive biological force fields. *J. Comput. Chem.* **31**, 671–690 (2010).

73. K. Vanommeslaeghe, A. D. MacKerell Jr., Automation of the CHARMM General Force Field (CGenFF) I: Bond perception and atom typing. *J. Chem. Inf. Model.* **52**, 3144–3154 (2012).

74. T. Darden, D. York, L. Pedersen, Particle mesh Ewald: An $N \cdot \log(N)$ method for Ewald sums in large systems. *J. Chem. Phys.* **98**, 10089–10092 (1993).

75. G. Bussi, D. Donadio, M. Parrinello, Canonical sampling through velocity rescaling. *J. Chem. Phys.* **126**, 014101 (2007).

76. H. J. C. Berendsen, J. P. M. Postma, W. F. van Gunsteren, A. DiNola, J. R. Haak, Molecular dynamics with coupling to an external bath. *J. Chem. Phys.* **81**, 3684–3690 (1984).

77. B. Hess, H. Bekker, H. J. C. Berendsen, J. G. E. M. Fraaije, LINCS: A linear constraint solver for molecular simulations. *J. Comput. Chem.* **18**, 1463–1472 (1997).

78. B. Roux, The calculation of the potential of mean force using computer simulations. *Comput. Phys. Commun.* **91**, 275–282 (1995).

79. S. Kumar, D. Bouzida, R. H. Swendsen, P. A. Kollman, J. M. Rosenberg, The weighted histogram analysis method for free-energy calculations on biomolecules. I. The method. *J. Comput. Chem.* **13**, 1011–1021 (1992).

80. M. Polymenidou, K. Stoeck, M. Glatzel, M. Vey, A. Bellon, A. Aguzzi, Coexistence of multiple PrP<sup>Sc</sup> types in individuals with Creutzfeldt-Jakob disease. *Lancet Neurol.* **4**, 805–814 (2005).

81. R. Zahn, C. von Schroetter, K. Wüthrich, Human prion proteins expressed in *Escherichia coli* and purified by high-affinity column refolding. *FEBS Lett.* **417**, 400–404 (1997).

82. D. A. Lysek, K. Wüthrich, Prion protein interaction with the C-terminal SH3 domain of Grb2 studied using NMR and optical spectroscopy. *Biochemistry* **43**, 10393–10399 (2004).

83. S. Hornemann, B. Christen, C. von Schroetter, D. R. Pérez, K. Wüthrich, Prion protein library of recombinant constructs for structural biology. *FEBS J.* **276**, 2359–2367 (2009).

84. A. C. Apetri, D. L. Vanik, W. K. Surewicz, Polymorphism at residue 129 modulates the conformational conversion of the D178N variant of human prion protein 90–231. *Biochemistry* **44**, 15880–15888 (2005).

85. A. Balguerie, S. Dos Reis, C. Ritter, S. Chaignepain, B. Coulary-Salin, V. Forge, K. Bathany, I. Lascu, J. M. Schmitter, R. Riek, S. J. Saupe, Domain organization and structure–function relationship of the HET-s prion protein of *Podospora anserina*. *EMBO J.* **22**, 2071–2081 (2003).

86. K. Almstedt, S. Nyström, K. P. Nilsson, P. Hammarström, Amyloid fibrils of human prion protein are spun and woven from morphologically disordered aggregates. *Prion* **3**, 224–235 (2009).

87. H. R. Büeler, M. Fischer, Y. Lang, H. Bluethmann, H. P. Lipp, S. J. DeArmond, S. B. Prusiner, M. Aguet, C. Weissmann, Normal development and behaviour of mice lacking the neuronal cell-surface PrP protein. *Nature* **356**, 577–582 (1992).

88. S. Nyström, R. Mishra, S. Hornemann, A. Aguzzi, K. P. Nilsson, P. Hammarström, Multiple substitutions of methionine 129 in human prion protein reveal its importance in the amyloid fibrillation pathway. *J. Biol. Chem.* **287**, 25975–25984 (2012).

Editor's Summary

**Putting prions in their place**

    In a mouse model of prion disease, Herrmann *et al*. evaluated the therapeutic efficacy of luminescent conjugated polythiophenes (LCPs), which are molecules with a high affinity for ordered protein aggregates. Intracerebral administration of LCPs into prion-infected mice using osmotic pumps increased survival. Solid-state nuclear magnetic resonance and in silico binding studies of LCPs to simplified model fibrils allowed the authors to define structural rules, which they then used for the design of LCPs with superior prophylactic and therapeutic potency. The new work demonstrates the feasibility of rational drug design for developing therapeutics to treat prion diseases.